

1N-26  
47314  
p. 87

# A Study of the Microstructure of a Rapidly Solidified Nickel-Base Superalloy Modified With Boron

James S. Speck  
*Massachusetts Institute of Technology*  
*Cambridge, Massachusetts*

November 1986

Prepared for  
Lewis Research Center  
Under Grant NAG3-365



National Aeronautics and  
Space Administration

(NASA-CR-179553) A STUDY OF THE  
MICROSTRUCTURE OF A RAPIDLY SOLIDIFIED  
NICKEL-BASE SUPERALLOY MODIFIED WITH BORON  
M.S. Thesis. Final Contractor Report  
(Massachusetts Inst. of Tech.) 87 p

N87-14486

Unclas  
G3/26 43743

## Table of Contents

Chapter		Page
	Acknowledgements . . . . .	ii
1	Introduction . . . . .	1
	1.1 Fundamentals of Nickel-Base Superalloys . . . . .	2
	1.2 Definition of Research . . . . .	4
2	Literature Survey . . . . .	6
3	Experimental Procedure . . . . .	13
	3.1 TEM Specimen Preparation . . . . .	14
	3.2 Transmission Electron Microscopy . . . . .	15
	3.3 Scanning Transmission Electron Microscopy . . . . .	15
4	Results . . . . .	16
	4.1 'Macroscopic' Structural Characteristics . . . . .	16
	4.2 Microstructure -- Transmission Electron Microscopy . . . . .	17
	4.3 Boundaries and Borides . . . . .	24
	4.4 Borides . . . . .	27
	4.5 Scanning Transmission Electron Microscopy . . . . .	28
5	Discussion . . . . .	29
	5.1 'Macroscopic' Features . . . . .	29
	5.2 Microstructural Features . . . . .	31
	5.3 Boundary Precipitation . . . . .	32
	5.4 Borides . . . . .	34
	5.5 Model for Lateral Microstructural Features . . . . .	35
	5.6 Chemical Analysis by STEM . . . . .	38
6	Summary and Conclusions . . . . .	40
7	Directions for Future Work . . . . .	42
	Bibliography . . . . .	44
	Appendix . . . . .	46
	Figures . . . . .	47

### Acknowledgements

I warmly thank Professor John Vander Sande for the guidance and expertise which he has provided. Without his efforts, this project would not have been possible.

Sincere thanks must be extended to Mr. Ernesto Gutierrez for several invaluable conversations dealing with fundamental aspects of melt-spinning.

The tireless assistance of Mr. Frode Stavehaug in preparation of the final document is greatly appreciated.

Mr. Jonathan S. Montgomery's assistance with experimental details and help with preparation of presentations and this document is greatly appreciated.

I must thank my officemates, Mr. Frank Gayle and Mr. Keith Taylor, for several stimulating conversations about this project and for their strong moral support.

Finally, financial support for this project has been partially provided by the NASA Lewis Research Center (NAG 3-365). The author's financial support since September 1984 has been provided by the National Science Foundation in the form of a graduate fellowship.

## 1. Introduction

The study of complex nickel-base superalloys has been referred to as "enlightened empiricism" (1). In the following work, I hope to add to our enlightened understanding of these materials and also draw conclusions about some of the fundamental processes occurring during solidification.

This study specifically deals with the microstructural evolution of three nickel-base superalloys of roughly the same base composition, but with differing boron levels. The materials were produced by rapid solidification processing (RSP) and specifically by melt-spinning. One of the primary advantages of utilizing melt-spinning is the ease in which experimental alloys can be produced. Conventional processing techniques would involve casting some sort of large ingot, then working the ingot to refine the macrostructure. Subsequently, several sections would have to be made and mechanically thinned to a size suitable for preparation for transmission electron microscopy. On the contrary, thin specimens suitable for final TEM preparation can be very quickly produced by melt-spinning.

With these experimental conveniences aside, there are several fundamental features of rapid solidification which cannot be overlooked. Due to the exceedingly high cooling rate of rapid solidification, on the order of  $10^3 - 10^8 \text{ Ks}^{-1}$ , significant structural refinement can be achieved. Cooling rates this high can be accomplished using processes such as melt-spinning, inert-gas-atomization, splat-quenching, or laser surface modification. The structural refinement is usually manifested as a very fine grain structure in which compositional fluctuations are limited

to the dimensions of the parent dendrite arm spacing. Further, a refined precipitate dispersion often results due to the compositional homogeneity. Large solute supersaturations are frequently obtained due to the short times the solid material resides at high temperature. Less frequently, new metastable phases are observed (2). Each of the individual effects described can provide desirable physical and chemical properties. Furthermore, the synergistic combination of these effects can lead to a highly desirable structure.

### 1.1 Fundamentals of Nickel-base Superalloys

Nickel-base superalloys have often been considered a crown-jewel of physical metallurgy. This, unfortunately, does not speak well for physical metallurgy as a hard science. At best, our understanding of the chemistry of these materials is based on insightful empiricisms rather than basic predictive models. Our knowledge of optimal processing conditions is based largely on trial and error. Perhaps our best understanding of these materials is in their mechanics which depend on chemistry in only an indirect manner. This should not cast a dark shadow, however, for it has precisely been through empirical developments that impressive advances in the service properties of these materials have been achieved.

The alloying scheme is to produce a structure which is mechanically strong, with high creep and fatigue resistance, good fracture toughness, and excellent hot corrosion resistance. To fit this demanding bill, a nickel matrix acts as a foundation upon which the alloy is built. Elements such as titanium and

aluminum are added to form an ordered coherent precipitate known as  $\gamma'$ . In nickel-base alloys  $\gamma'$  has a composition of  $\text{Ni}_3(\text{Al}, \text{Ti})_1$ , which is isomorphous with the  $\text{Cu}_3\text{Au}_1(\text{Li})_2$  structure. Further alloying by elements such as chromium and molybdenum provide solid solution strengthening in the austenite. The aluminum and chromium provide essential corrosion resistance by doubling as coherent oxide formers. Interstitial elements may be added to form grain boundary phases which retard grain growth and, to a lesser extent, provide resistance to boundary sliding. In the alloys used for this study, boron was added to modify boundary structure.

Grain size and boundary structure are principle features in any microstructure. From the Hall-Petch relation it is known that yield strength is inversely proportional to the square root of grain size. Incoherent precipitates provide local minima in interfacial area when straddled by a grain boundary. Hence, incoherent precipitates act as effective barriers to curvature driven boundary migration. The coherent  $\gamma'$  precipitates are much less effective boundary pinners than incoherent precipitates because when a high energy, high-angle boundary straddles a coherent precipitate there can be no reduction in effective high-angle boundary area. The superalloys, principally used in high temperature applications, often must be alloyed to form incoherent grain boundary precipitates.

Mechanical properties and the effects of boundary structure must also be considered. Sufficiently stressed materials at high temperatures will flow viscously, or as is more commonly known,

they will creep. In polycrystalline materials, the reduction in potential energy can be achieved either by mechanical deformation (usually dislocation motion) or by diffusive processes. In either case boundary accommodation must occur and is usually manifested as grain boundary sliding. Boundary sliding is a diffusive process and the presence of discrete boundary precipitates will weakly retard the process (3). Fatigue damage is a second consideration. Cyclic loading often leads to void formation at grain boundary precipitates. Void coalescence and localized overload can lead to catastrophic failure. So we see that grain boundary precipitates provide the beneficial effects of controlling grain size and reducing sliding, but unfortunately promote boundary damage such as creep and fatigue cavitation and cracking.

## 1.2 Definition of Research

In this work, the microstructure of a melt-spun nickel-base superalloy was studied exclusively by electron microscopy. The structure of the material will be considered as a function of both boron level and location through the ribbon thickness. Particular attention will be paid to grain shapes and boundary morphology as these topics have not been properly elucidated by others. In this regard, the microstructure of melt-spun ribbons, for at least one class of alloys, will be more thoroughly understood.

The alloys are of approximate composition Ni-11%Cr-4%Mo-5%Al-4%Ti with boron levels varying from 0.12% to 0.60% (all compositions by weight). The alloy chemistry is simpler than

most commercially available superalloys, but it nevertheless mimics the structural features of commercial alloys. In this regard, the material is more easily understood than a complex system with eight or nine alloying elements. Boron has been selected as the grain boundary phase former because its phases in this material tend to be chromium and molybdenum rich, but depleted in aluminum and titanium. This leaves titanium and aluminum free to form  $\gamma'$  precipitates and reduces the possibility of  $\gamma'$  depleted zones adjacent to boundary precipitates. In addition, borides do not seem to undergo decomposition reactions that carbides often experience. Finally, melt-spun material was chosen because of the potential for structural refinement by rapid solidification and for the inherent simplicity in production.

## 2. Literature Survey

This chapter provides a brief overview of relevant literature pertaining to rapid solidification in general, specific work on rapid solidification of nickel-base superalloys, and the role of boron in complex heat-resistant alloys. In no way is this chapter intended to be an exhaustive survey of any of the above fields. Rather, the intention is to show that the current study will both complement and contribute to the body of knowledge of rapid solidification of heat-resistant alloys, and more broadly, solidification of crystalline materials.

For nearly twenty-five years now there has been a large research effort in the area of rapid solidification. During the 1960's a great deal of research was performed to explore the variety of structures attainable by quenching liquid metal at rates as high as  $10^9 \text{ Ks}^{-1}$ . It was observed that significant structural modifications could be obtained for the crystalline state. Such modifications included significant refinement of grain size, large supersaturations of solute, fine dispersions of second phase particles, and new metastable phases. Each of these features is of either great technological or scientific importance. For an in-depth review of the first decade of rapid solidification, the reader is referred to the review article by Anantharaman and Suryanarayana (4).

During the 1970's and early 1980's structural explorations continued. In addition, numerous research efforts were undertaken to understand the underlying processes of rapid solidification. In an extensive review article, Jones (5) considers the effects of experimental variables on resulting structures and

properties. Jones' review deals primarily with research published in the early 1970's--reflecting the efforts during this period for a more basic understanding of process variables on final structure. Cohen and Mehrabian (6) discuss basic aspects of the relationships between supercooling, heat transfer, and microstructure in a detailed review. The models developed seem most successfully applied to small powder particles. In a less extensive article, Cohen, Kear, and Mehrabian (7) provide a broad overview of the fundamental concepts and technological processes of rapid solidification. Discussions of commercial and experimental methods for producing rapidly solidified materials, as-cast microstructures, cooling rate and thermal gradients effects are included. This article represents an excellent starting point for a newcomer to the field. Our focus will now shift to alloy-system-specific research.

During the past several years many research groups have realized the potential for structural refinement of commercial alloys by rapid solidification processing (RSP). Because of obvious technological implications, numerous microstructural studies have been performed on materials produced by powder processes. Fewer studies have been performed on melt-spinning of commercial alloys because of the inherent difficulties with ribbon consolidation. Here, attention is focused on melt-spun superalloy ribbons.

One of the first such studies was performed by Wood et al (8). Both 'macrostructural'\* and microstructural features of

---

\*By macrostructural, it is meant that features on a size scale similar to casting dimensions are considered.

-----  
melt-spun Nimonic 80A were studied. The macrostructure was found to have three distinct regions; homogeneous grains near the wheel side, a cellular structure in the ribbon center, and a branched dendritic structure near the free surface. Near the wheel side, polygonization of the internal dislocation structure was observed along with precipitation of titanium carbide at cell boundaries. Further, it was shown that for grains near the wheel side, the angular mismatch between adjacent grains was often 'small.' The authors suggested the low-angle boundary structure was due to a heat flow effect during solidification. Bright field/dark field microscopy was not employed to further investigate this effect--if it had been employed, true grain shapes would have been elucidated. The remainder of the study was concerned with precipitation of matrix phases.

A more comprehensive study was provided by Davies et al (9). Both macrostructural and microstructural features of four commercial melt-spun superalloys were studied. Two distinct zones were observed in the macrostructure; a fine chill zone near the wheel side and a columnar dendritic zone in the ribbon center and near the free surface. The columnar dendritic grains were inclined about  $20^\circ$  to the ribbon normal. Unfortunately, Davies et al mistakingly reversed the orientation of the inclination by assuming it was opposite to the casting direction which is contrary to flow considerations and results of other investigators (10, 11, 12, 13). Near the wheel side of all of the alloys studied, carbides with a parallel orientation relationship lined both cell

walls and grain boundaries. The structure became either dendritic or columnar in the center and at the free surface of the ribbon, again boundary precipitates were observed. However, no bright field/dark field microscopy was performed to determine the true extent of any grains or the boundary morphology.

Structure is inherently a function of processing history. In this manner, Duflos and Stohr (14) directly compared microstructures of gas-atomized and melt-spun cobalt- and nickel-base superalloys. Although their study primarily dealt with cooling rate considerations, included are figures depicting macro-features and several micrographs of structure as a function of location in the ribbons. For our purposes, this study is important for two reasons. First, the study clearly shows the differences in microstructure of melt-spun ribbons and gas-atomized powders. The critical lesson to be learned is that for alloy development purposes, experimental processing conditions should closely mimic final large-scale processing conditions lest one be working with a material of coincidental composition but entirely different structure. Second, examples of microstructures as a function of location through the ribbon thickness are given. Again, three characteristic regions were observed for both types of alloy systems; a featureless chill zone near the wheel side, a columnar dendritic structure in the ribbon center, and randomly oriented dendrites near the free surface. In the systems studied (HS-6 -- a cobalt-based alloy, and C-146 -- a nickel-based alloy), carbide precipitates decorated grain boundaries. Again no effort was made to rigorously define grain shapes and boundary morphologies.

Solid state nucleation of second phase particles and structural development were considered in an experimental nickel-base superalloy by Huang and Ritter (15). The alloy studied is similar to Rene 120 but with a much lower carbon level. 'Macroscopically,' the same three distinct zones were observed as discussed previously. The microstructure also showed similar characteristics to those discussed previously. Huang and Ritter made the implicit assumption that the grains at the wheel side were monocellular and proceeded to calculate a nucleation density from the measured cell size. The assumption of monocellular grains is justified only if several sets of bright field/dark field pairs are recorded--none were presented in Huang and Ritter's work.

#### Boron

Since the late 1950's, boron has been known to improve the creep, rupture and intergranular fracture properties of nickel-base alloys. Direct evidence for boron segregation to grain boundaries in coarse-grain nickel-base superalloys has been obtained by autoradiography and secondary ion mass spectrometry (16, 17, 18). The lateral resolution of these techniques is on the order of several microns which effectively prohibits their use for RSP materials.

Boron is known to suppress boundary nucleated phase transformations in iron-based alloys (19). It is suspected that boron locally reduces austenite free energy, hence reducing the driving force for a phase transformation. Ruhl and Cohen (20) determined that increasing levels of boron in iron-nickel-boron splats dramatically increased the volume fraction of retained austenite.

This again suggested that boron stabilizes austenite grain boundaries with respect to transformation. One can clearly see that parallel effects are possible in nickel, particularly since austenitic iron and nickel form a continuous solid solution at high temperatures. Boron is an unusual element, with many grain boundary segregants the total internal energy of the system is raised. With boron, however, it appears that the total energy of many systems is decreased by its presence.

During the 1950's and 1960's superalloy development was at an apex. Boron and zirconium were discovered to improve the creep properties of nickel-base superalloys. In their classic paper, Decker and Freeman (21) described results of a microstructural investigation on crept boron-modified nickel-base superalloys. It was determined that boron retarded microstructural degradation of grain boundaries (cavitation and cracking). Decker and Freeman stated that the mechanism of improved creep properties was due to the "stabilizing effects of traces of boron and zirconium on the alloys." Although this may be mechanistic in the classical sense, it still leaves one searching for a satisfactory microscopic or 'atomistic' explanation for boron's effects.

Fundamental approaches to metallurgical phenomena are difficult because of the inherent complexity of such problems. One 'first principles' technique has been successfully applied to many such problems though, that is, self consistent field (SCF) molecular orbital calculations (22). Messmer and Briant (23) applied SCF techniques to determine energy eigenvalues and charge

density distributions for tetrahedral clusters of iron and nickel with either a sulfur, phosphorus, carbon, or boron atom residing in the tetrahedron center. It was determined that sulfur formed homopolar bonds with the metal host, hence reducing charge density for adjacent metal-metal bonds. Sulfur therefore weakens the metal matrix. On the other hand, boron formed heteropolar bonds with the surrounding metal host and actually acts as a cohesive enhancer. These results are consistent with observed macroscopic results.

When boron is alloyed in higher levels than implied in the previous discussion, boride precipitation must be considered. For a long review on borides of transition elements, the reader is referred to the work of Kiessling (24) or that of Nowotny (25). In the late 1960's Boesch and Canada (26) analyzed electrolytic extractions of all the phases present in Udimet 700. The boride phase was determined to be of the type  $M_3B_2$ . This boride type is the one most frequently encountered in nickel-base superalloy systems.

During the 1950's boron was added to many alloys. In 1958 Beattie (27) performed the original crystallographic work on the  $M_3B_2$  phase. Electrolytically extracted precipitates from HS-88 and IN-901 were studied. The only boron-bearing phase was  $M_3B_2$ . A crystallographic analysis revealed that the borides were tetragonal with an a-axis of 5.7 Å and a c-axis of 3.1 Å. The precipitates belong to the space group  $P4/mbm$ . Additionally, the  $M_3B_2$  phase turns out to be isomorphous with  $U_3Si_2$ . As we will see later, crystallographic factors play strongly in solidification scenarios.

Finally, this section is closed with a discussion of the work of Huang, Hall, and Glasgow on identical alloy systems and processing conditions used for the current study (see the following section for details on composition and processing). As a brief summary, the following results were obtained:

- Bend ductility of the ribbons decreased with increasing boron levels.
- Alloy 71 had a center cell size of 0.5 microns.
- Electron diffraction studies on annealed borides yielded the following orientation relationships:

(001) matrix // (001) boride  
[001] matrix // [001] boride  
(100) matrix // [310] boride

- As-cast electrolytically extracted borides of alloy 72 had lattice parameters  $a = 5.67 \text{ \AA}$ ,  $c = 3.05 \text{ \AA}$ . Energy dispersive x-ray analysis on the extracted borides yielded the following:

strong peak: Mo, Cr  
moderate peak: Ni  
weak peak: Ti

This suggested a  $(\text{Cr}, \text{Ni})_2 (\text{Mo}, \text{Ti}) \text{B}_2$  boride.

Many inroads to understanding these alloys were made by Huang, Hall, and Glasgow in their study. For the purpose of the current investigation, knowing the boride chemistry and orientation relationship with the matrix will prove extremely useful. Their study on the as-cast system is nevertheless far from complete. The microstructures in the three characteristic regions have not been documented. Grain shapes and boundary morphologies have not been examined. So it can be easily seen that there is room and necessity for further examination of these alloys.

### 3. Experimental Procedure

#### **Ribbon**

Melt-spun ribbon was graciously supplied by the NASA Lewis Research Center. All samples for this study were prepared at the General Electric Research Laboratory.

Ribbons with approximate thickness of 30  $\mu\text{m}$  and 5 mm width were produced in vacuum by the planar flow melt-spinning process. The alloy compositions are given as follows (all in weight per-cent):

<u>Alloy #</u>	<u>Ni</u>	<u>Cr</u>	<u>Mo</u>	<u>Al</u>	<u>Ti</u>	<u>B</u>
70	77.34	10.50	3.05	5.16	3.94	0.012
71	76.49	10.60	3.73	5.10	3.96	0.12
72	72.69	11.07	6.75	4.82	4.07	0.60

#### **3.1 TEM Specimen Preparation**

Electron transparent specimens were prepared for samples near the wheel side (WS), in the ribbon center (C), and near the free surface (FS).

3 mm discs for TEM were produced either by punching or ultrasonically cutting with a silicon carbide slurry. Generally, no mechanical thinning was necessary. A 20% perchloric acid--80% methanol solution was used for final thinning. The electrolyte was immersed in a dry ice--methanol solution. Solution temperatures, measured in the electrolyte, ranged from  $-65^{\circ}\text{C}$  to  $-70^{\circ}\text{C}$ . All thinning was performed on a Fiscione jet thinning apparatus. The operating potential ranged from 10 to 20 volts.

Specimens from the ribbon center were prepared by dual sided thinning to perforation. This procedure produced sufficient thin

area for microscopy.

Specimens from the ribbon free surface and wheel side were prepared by thinning for 1 minute on both sides (to remove handling damage), then removing the specimen from the solution and placing a thin piece of polyethylene over one surface of the sample. This was followed by resumed jet thinning with two jets, but with only one exposed surface being thinned. Generally, after this step there was insufficient thin area for electron transparency. Hence, these specimens were ion-milled for 4-12 hours with  $\text{Ar}^+$  ions accelerated across a potential difference of 6 KV. Ion incidence angle on the specimen was always  $10^\circ$ . Gun currents ranged between 0.5 to 1.0 mA.

### 3.2 Transmission Electron Microscopy

A small fraction of the microscopy for this study was performed using a Philips EM-300 transmission electron microscope operating at 100 KV. The majority of the work was performed on a JEOL 100CX TEM operating at 100 KV using a eucentric double tilt holder.

### 3.3 Scanning Transmission Electron Microscopy

All analytical work for this study was performed on a Vacuum Generators HB-5 STEM operating at 100 KV. Chemical analysis was performed using an energy dispersive x-ray analyzer (EDXA) coupled with commercially available analytic software. Chemical analysis for light elements was performed by electron energy loss spectroscopy (EELS).

## 1. Results

Results of all experimental studies will be presented in this section. Any substantive discussions of the results will be delayed until the following section.

### 4.1 'Macroscopic' Structural Characteristics

For the context of this study only, 'macroscopic' features are to be considered those features that are on the size scale of the thickness of the casting. For these 30  $\mu\text{m}$  thick ribbons, scanning electron microscopy (SEM) turns out to be the ideal tool. 'Macroscopic' structure is presented primarily to provide a context in which the transmission electron microscopy can be presented. All SEM work and associated sample preparation was performed by H. Segal (29).

To begin, the longitudinal structure of alloy 70 is shown in fig. 1. In this micrograph the wheel side of the ribbon is at the bottom of the page, the free surface at the top. Casting direction is from left to right. Three characteristic structural regions are observed. Near the wheel side an essentially featureless 5  $\mu\text{m}$  thick region is seen. Moving up through the ribbon thickness, the featureless region is seen to develop into a distinct columnar structure in the ribbon center. The columnar structure begins to break down into a dendritic structure in the top 5  $\mu\text{m}$  of the ribbon. Secondary dendrite arms are observed near the free surface. It should also be noted that there is approximately a 10° to 20° tilt of the columnar structure into the casting direction. A mental note should be made that alloy 70, the low boron alloy, represents a reference point or control

for this study.

The effects of increasing boron level can be seen in the longitudinal section of alloy 71, which is shown in fig. 1. Here again three characteristic structural regions are observed. However, the featureless region near the wheel-side is much smaller than in alloy 70, in this case only about 2  $\mu\text{m}$ . The columnar structure extends from the featureless wheel side region to within about 10  $\mu\text{m}$  of the free surface. Near the free surface a developed dendritic structure is observed and secondary dendrites are easily seen. Again, tilting of the columnar dendritic grains into the casting direction is prevalent.

The effects of further boron additions are seen in the longitudinal structure of alloy 72, shown in fig. 3. The sample configuration is the same as that shown in fig. 1. In this case only two characteristic regions are observed. The 10  $\mu\text{m}$  of material near the wheel side displays features of a broken-up columnar dendritic structure. The structure begins to become more columnar-like near the ribbon center, but this is convoluted by the presence of secondary dendrite arms locally. The upper half of the specimen is fully dendritic. There is also a noticeable tilt of the columnar dendritic structure into the casting direction. In comparison with the structures of alloys 70 and 71, a substantial degree of refinement is observed.

#### 4.2 Microstructure -- Transmission Electron Microscopy

In this section, several sets of bright field/dark field (BF/DF) pairs will be considered. For each alloy, BF/DF pairs for specimens prepared near the wheel side (WS), center (C), and

free surface (FS) will be discussed. In addition, several micrographs of general structure will be considered. Overall grain shapes and subgrain structure will be elucidated in this manner.

Two disclaimers must be made prior to presenting more results. The first is that little distinction will be made between subgrains and cells. The former is associated with structures resulting from dislocation rearrangements and the latter with structures resulting from instabilities at the liquid-solid interface. Differentiation between the two structures is difficult, in this case, due to the fast kinetics of solidification. Secondly, gamma prime precipitates turn out to be of little significance for this study and hence will not be considered in any detail.

For all of the bright field/dark field pairs presented, a two-beam condition was established in reciprocal space for the grain of interest. This grain will be referred to as either the reflecting or diffracting grain.

To start off, the structure of alloy 70 is considered. The general structure of the alloy near the wheel side is shown in fig. 4. The approximate mean-intercept grain size is  $1.5 \mu\text{m}$  (no rigorous grain size determination has been carried out for reasons discussed later). The boundaries are slightly wavy, but no regions of large curvature are observed. The grains all appear to have convex<sup>\*</sup> shapes. Within several of the grains a sort of

---

\* A convex polygon is one in which a line connecting any two interior points never passes through an exterior region of the polygon. A concave polygon is a polygon in which it is possible to have a line which connecting interior points pass through a region exterior to the polygon.

---

cellular pattern is observed. And finally it must be noted that no boride precipitation is observed. A BF/DF pair from the wheel side of alloy 70 is shown in fig. 5. In this instance there is some curvature to the boundaries and two subgrains are observed to constitute the reflecting grain. The smallest radius of curvature, roughly  $0.5\text{ }\mu\text{m}$ , is mild and occurs at an absolute triple point.\* Finally, careful examination of figures 4 and 5

-----  
\*An absolute grain boundary triple point is the contact point of three grain boundaries regardless whether the boundaries are high- or low-angle.  
-----

-----  
show the large volume fraction of  $\gamma'$  precipitate in the structure.  
-----

Moving up to the center of alloy 70, the general structure is nearly identical to the general structure near the wheel side. In the BF/DF pair shown in fig. 6, it can be seen that the reflecting grain has no subgrain formation. Further, the boundaries are very straight, and the polygon formed by the grain boundaries is convex. As for all cases presented within, it must be emphasized these are only representative structures and in all cases there will be a distribution for the amount of subgrain formation.

The overall structural appearance at the free surface of alloy 70 is the same as that near the wheel side. There are great differences, however, in the amount of subgrain formation, this is depicted in the BF/DF pair shown in fig. 7. This particular example shows that there can be extensive subgrain formation, here at least four subgrains exist. Grain size increases substantially when subgrains are considered. The reflecting grain in fig. 7 is roughly  $4\text{ }\mu\text{m}$  in diameter. The overall boun-

dary structure is wavy and forms a concave polygon. Careful examination of fig. 7 reveals that minima in boundary amplitude\*

-----  
\*For a discussion of 'boundary amplitude,' see appendix 1.

-----  
occur at absolute triple points. Other elements of the structure near the free surface of significance include the apparent absence of boride precipitates and the low dislocation density within individual subgrains. From these results it can be seen that for alloy 70 boron is at least metastably soluble and its role in the development of the microstructure is limited to soluble segregation and interfacial energy modifications.

Marked changes in the microstructure of the base alloy are observed when boron levels are increased. To begin, the general structure of alloy 71 ( $C_B = 0.12\%$ ) near the wheel side is considered. The microstructure, shown in fig. 8, displays boride precipitates dispersed along nearly all of the boundaries and only at boundaries. The apparent grain size is much smaller than in alloy 70, in this case only  $0.5\ \mu\text{m}$ . The borides are approximately  $100 - 200\ \text{\AA}$  in diameter and spaced about  $2000\ \text{\AA}$  apart in the thin foil. Dark field microscopy, using matrix reflections, reveals that there is limited subgrain formation. The BF/DF pair shown in fig. 9a gives an example of a grain with two or three subgrains. The boundary structure is rough and forms a concave polygon. Local minima in boundary amplitude occur at absolute boundary triple points. Another BF/DF pair from the wheel side of alloy 71 is shown in fig. 9b. No subgrain formation is observed for the reflecting grain in the figure. The grain boundaries are fairly straight and boride precipitates are

observed only along the high-angle boundaries. Also included in fig. 9b is a  $\gamma'$  dark field image formed using a (100) superlattice reflection. The coherent ellipsoidal  $\gamma'$  precipitates are roughly 100 Å in diameter. Boride precipitation is the first notable structural alteration caused by increases in boron level.

The microstructure of alloy 71 is modified in several ways in the ribbon center. A typical structure is shown in the BF/DF pair of fig. 10. The overall grain shape of the reflecting grain is irregular. To assist the reader, the boundary shape has been outlined in the figure. From the boundary outline, local radii of curvature as small as 0.2  $\mu\text{m}$  can be measured. Local minima in boundary amplitude are again observed at absolute triple points. Boride precipitation is readily observed at both low- and high-angle boundaries. Local regions of high dislocation density surround each low angle boundary precipitate. These accommodation or antioherency dislocations are observed only at low-angle boundaries. Finally, the overall grain in question measures approximately 2  $\mu\text{m}$  across, with each subgrain having dimensions of approximately 1  $\mu\text{m}$ . The borides are approximately 100 to 200 Å in diameter.

Structural alterations near the free surface of alloy 71 are similar to those observed in the center. Two sets of BF/DF pairs are presented in fig. 11 for microstructures near the free surface of alloy 71. These structures are characterized by extensive subgrain formation. In fig. 11a, we see a grain "lighting up" in dark field with seven subgrains. The overall grain shape is concave and again minima in boundary amplitude are observed to occur at absolute triple points. The grain faces have some wave

or curvature. Careful examination of the boundary structure reveals that the boride size is smaller at low-angle boundaries than at high-angle boundaries. In general, though, boride density is greater at the low-angle boundaries. One additional observation should be made for this figure; the subgrain in the lower right of the figure is an example of cellular solidification. This subgrain is contiguous with the adjacent subgrain by a path around the cell boundary. Another example of the structure of alloy 71 near the free surface is given in the BF/DF pair of fig. 11b. The same general comments apply to this figure. Here, eight subgrains constitute the reflecting grain. Comparing the microstructure of alloys 70 and 71 shows that boron enhances subgrain formation and the formation of irregular grain shapes.

The effects of further boron modification can be seen in the structure of alloy 72. The structure near the wheel side is shown in the BF/DF pair of fig. 12a. In this example, two separate grains "light up" in dark field when using a (200) matrix reflection. Both reflecting grains consist of two subgrains. The overall grain shape is concave. There are a few minima in boundary amplitude not associated with absolute triple points. There also appear to be intragranular regions with high local boride density. It should also be noted that the grains which "light up" in dark field are only about  $0.4\text{ }\mu\text{m}$  across. The boride precipitate size ranges from about 100 to 500 Å in diameter. The structure in any region of the ribbon (wheel side, center, and free surface) is not necessarily homogeneous due to local variations in casting conditions. Another BF/DF pair from

the wheel side of alloy 72 is presented in fig. 12b. In this case the structure is fully dendritic. A very unusual grain shape is observed for the grain "lighting up" in dark field. Subgrain or cell formation, however, is difficult to distinguish due to the presence of boride precipitates. A comparison of figures 12a and 12b verifies the lateral heterogeneity of the structure.

The structure in the center of alloy 72 becomes very dendritic as depicted in fig. 13. Dendritic solidification is inferred by local regions of high intragranular boride precipitate density and star-shaped precipitate free regions. Again individual grain shapes are unusual as depicted in the BF/DF pair of fig. 14a. In this figure, a star-shaped primary dendrite is surrounded by interdendritic regions of high boride density. On the outer peripheries of the reflecting grain there are three circular precipitate free regions. These regions are also probably primary dendrites which have not developed lateral shape perturbations. Another example of the grain structure in the center of alloy 72 is shown in fig. 14b. In this case, the subgrain-cellular structure is more easily depicted than in fig. 14a. Again the overall grain shape is concave and there are local minima in boundary amplitude not associated with triple points. One intragranular region is observed to have high boride density. The grain size in the center of alloy 72 ranges from about 0.5 to 1.0  $\mu\text{m}$ .

The structure at the free surface of alloy 72 becomes fully dendritic as shown in fig. 15. From this general structure, it can be seen that there are primary, secondary, and probably

tertiary dendrite arms in the structure. Again, the interdendritic regions show a high density of boride precipitates. The grain shapes are highly irregular as depicted by the BF/DF pairs of fig. 16. A structure in which the high-angle boundaries are almost completely decorated with borides is shown in fig. 16a. The reflecting grain is approximately 1  $\mu\text{m}$  across. A portion of a much larger grain is shown in fig. 16b. The total grain consists of at least eight subgrains. The most striking features of the reflecting grain are the two boundary regions with large inward curvature. In one case, the radius of curvature is 0.2  $\mu\text{m}$  locally. A large band of boride precipitates is observed to run across the grain. The borides in the region to the left of the reflecting grain are also of interest. Careful inspection shows that these precipitates are ellipsoidal with major axes running in one of two perpendicular directions. The borides measure approximately 300 - 500 Å along their major axis and have a ratio of semiaxes of about two.

#### 4.3 Boundaries and Borides

Our focus now turns to the structure of both low- and high-angle grain boundaries in these alloys. This in turn will lead to results of structural studies on the boride precipitates.

Recalling the results of the previous section, it was found that the microstructures of alloy 70 near the wheel side and in the center consisted of convex grains with straight boundaries and no boride precipitation. A closer examination of the boundary structure in the center of alloy 70, presented in fig. 17, shows straight, precipitate free high-angle boundaries. All

results for boundaries of alloy 70 near the wheel side and in the ribbon center indicate clean and 'quiet' boundaries.

The low- and high-angle boundaries of alloy 70 near the free surface are also straight and featureless. Some of the low-angle boundaries, nevertheless, display a fine speckled structure as shown in fig. 18. This structure may simply be due to dislocation contrast or perhaps a very fine dispersion of boride particles 50 to 100 Å in diameter. This figure represents the 'noisiest' boundary in any region of alloy 70.

The boundary structure of alloy 71 becomes considerably more complex due to the presence of both low- and high-angle boundaries and a substantial number of borides. Examination of several sets of micrographs of both low- and high-angle boundaries indicates that the high-angle boundaries have larger precipitates than the low-angle boundaries, but the low-angle boundaries contain a higher density of precipitates. An example of the difference between the two types of boundaries is shown in fig. 19 for an area in the ribbon center of alloy 71. The low-angle boundary boride precipitates are all seen to interact with dislocations. The high-angle boundary borides are all discrete, resolvable and, other than the boundary itself, have no interfacial dislocation structure.

Near the free surface of alloy 71, the differences in low- and high-angle boundary structure are more easily resolved. Such is the case for the microstructure presented in fig. 20a. The boundaries marked 'high-angle' are lined with borides approximately 600 Å in diameter, whereas the low-angle boundaries dis-

play a nearly continuous string of precipitates approximately 300 Å in diameter. A detailed view of one of these low-angle boundaries is shown in fig. 20b. Here the boundary has a rope-like appearance. Several factors may contribute to the contrast in this image; first there is the inherent dislocation structure of the low-angle boundary, second, there is structure factor contrast associated with the boride precipitates. Shortly we will see that the borides have an orientation relationship with the matrix. This leads to the possibility of an interfacial (anticoherency) dislocation structure and elastic strain fields (coherency dislocations)--both can contribute to image contrast. So it can quickly be seen that the boundary structure in the boride-precipitating alloys is often complex.

Further increases in boron level, manifested as alloy 72, lead to such high boride density that differentiation of low-angle boundaries becomes difficult. So instead attention is focused on the borides. Interdendritic borides from a region near the wheel side of alloy 72 are shown in fig. 21a. Close examination of the borides reveals apparent moire fringe contrast, though this cannot be simply distinguished from an interfacial dislocation structure. For these interdendritic regions, the borides are approximately 150 - 350 Å in diameter with spacings on the order of their size. Another example of regions with high boride density is shown in fig. 21b, this time in the center of alloy 72. Again interdendritic regions with high boride density are observed. Of greater interest, though, is the upper boundary in the center of fig. 21b. Here the boride precipitates seem to fan out from the boundary. This suggests heterogeneous

nucleation of the precipitates at the grain boundary. The exact nature of the nucleation site for any of the borides has yet to be determined though.

#### 4.4 Borides

To begin, it must be stated that virtually all of the research herein on the borides is supplementary to work performed by other investigators (20).

The initial study on this system yielded information on boride crystal structure, chemistry, and orientation relationship with the surrounding matrix. These results are summarized in the literature survey. The interested reader is referred to that chapter for details.

All work by other investigators on boride crystallography and orientation relationships are consistent with the results of this study (schematic diffraction patterns are shown in fig. 22).

One additional orientation relationship between the matrix and the borides was observed infrequently:

(011) matrix // (001) boride  
{011} matrix // {001} boride

Finally, a phase different than  $M_3B_2$  gave rise to planes of 5.2 Å spacing parallel to (001) in the austenite matrix. A 5.2 Å interplanar spacing does not correspond to that of any common boride.

#### 4.5 Scanning Transmission Electron Microscopy

Two analytical methods have been applied to these alloy systems. Electron energy loss spectroscopy was used to verify

the presence of boron in the boundary precipitates. Energy dispersive x-ray analysis was used to determine general trends in compositional heterogeneity. A commercially available software program was used for background subtraction of all x-ray spectra. No quantitative analysis was performed due to the number of elements in these alloys. The following results reflect trends in ratios of individual element counts to total counts, after background subtraction, for a given region.

Alloy 70 - Slight (10 - 20%) enrichment of molybdenum and chromium to both low- and high-angle boundaries.

Alloy 71 - Slight (5 - 10%) depletion of molybdenum and chromium at grain boundaries.

- Chromium- and molybdenum-rich borides
- No significant variation in concentration of alloying elements as a function of location in the ribbon thickness.

## 5. Discussion

In this section, an effort will be put forth to understand all of the structural features presented thus far.

### 5.1 'Macroscopic' Features

The through thickness structural features for this alloy are analogous to macroscopic features in a large scale casting. For the large scale casting, a chill zone, columnar zone, and equiaxed zone are often observed. This, too, is the case with many ribbon castings. The featureless or equiaxed zone adjacent to the wheel side is essentially a chill zone. The analogy between columnar zones is completely coincident. The dendritic structure observed in the melt-spun ribbons can be considered as an extended perturbation of the columnar structure. The absence of a free surface equiaxed zone in the ribbons can be attributed to the finite dimensions of the castings. At least for the ribbons used for this study, there appears to be no scaling law for casting structure.

Structural features in all castings can be varied by altering alloy composition. Structural modifications were achieved in alloys 70 through 72 by varying the boron level. Reexamination of figures 1, 2, and 3 shows that increasing the boron level in these alloys enhances dendrite formation and causes structural refinement. Boron in these materials resides either in substitutional or interstitial sites and tends to be a strong boundary segregant. During solidification, the boron is most likely rejected from the freezing solid. The boron-rich liquid leads to enhanced constitutional supercooling and thus provides a more

favorable environment for dendritic freezing. With this simple line of reasoning, the 'macrostructure' of alloys 70, 71, and 72 can be understood. The structural refinement observed in these alloys may be attributed to a refined dendritic structure, as seen in alloy 72, and the possibility of solid state grain boundary pinning by boride precipitates. Boundary pinning will be considered in detail shortly.

Another interesting 'macrostructural' feature is the observed tilt of the columnar/dendritic structure into the casting direction. This result is counterintuitive because growth is anticipated normal to isotherms. Growth normal to isotherms leads to tilting of the columnar dendritic structure away from the casting direction. There are more subtle aspects of the freezing process which, when considered, account for the observed tilting.

Consider for a moment the fluid flow aspects of melt-spinning. A stream of liquid metal falls from a crucible onto a cold spinning substrate, schematically shown in fig. 23. A pool forms on the wheel. Downstream from the pool, solid begins to form as a thin strip. For a finite distance there is a layer of liquid above the solid. The solid and adjacent liquid have parallel velocity vectors. The speed of the solid is greater, however, due to viscous drag of the liquid. Hence, the solid effectively experiences liquid flow opposite to the casting direction. The net flow sweeps both the heat of fusion and solute to the trailing edge of a protrusion at the liquid-solid interface (10, 11, 12). This leads to dendrites or columnar grains at the liquid-solid interface which are cooler and purer in the casting direc-

tion and hence growth is favored in this direction. Tilting of the grain structure into the casting direction is a common feature for many melt-spun ribbons.

## 5.2 Microstructural Features

The microstructure of a nickel-base superalloy is complex and a simple understanding is often not at hand. In this section, trends in the microstructural evolution of alloys 70, 71, and 72 will be discussed. Specific microstructural features will be discussed in the following two sections. And in the fifth section, a model for lateral solidification associated features will be presented.

The microstructure of alloy 70 represents the simplest structure in this series of alloys. The boundaries are straight and precipitate free. Very little subgrain formation is observed near the wheel side or in the ribbon center. It is only near the free surface that subgrain formation is observed. It is plausible that near the free surface the cooling rate is sufficiently low, as calculations indicate (30), to allow for weak lateral solute segregation and development of a cellular structure. In essence, the formation of a subgrain structure near the free surface can only be rationally explained by a cellular solidification model. It is doubtful that the observed subgrain structure resulted from fast alignment of transformation dislocations during cooling, particularly since many of the 'solidification' dislocations are produced as a result of thermal stresses in the solid state. Needless to say, though, the mechanistics of subgrain formation in alloy 70 will not be determined by 'back of

the envelope' arguments.

The increased complexity of the microstructures of alloys 71 and 72 can be directly attributed to increased boron levels in these alloys. Recalling the results presented in the previous chapter, it was shown that there was little subgrain development near the wheel side of alloys 71 and 72, but the microstructures became either very cellular or dendritic in the center and near the free surface of the ribbon. Calculations performed by Gutierrez (30) have shown that the cooling rate near the free surface for these alloys is a factor of twenty lower than the cooling rate near the wheel side.

The following solidification scenario is proposed which takes into account both cooling data and structural results presented herein. The initial zone of solid forms very quickly with a random orientation, this is also the case with a large-scale casting. Thermal and compositional gradients are immediately established in the liquid. Grains with optimal orientation, primarily those with  $\langle 100 \rangle$  tilted about  $10^\circ - 20^\circ$  into the casting direction, begin to outgrow grains with unfavorable orientations. Interfacial instability occurs and either cellular or dendritic solidification follows. It must be remembered that several cells or primary dendrite arms can form from a single grain. The resulting cells or dendrites also grow competitively which further refines the growth texture of the ribbon. This solidification model, though generic in nature, is consistent with the observed microstructure.

### 5.3 Boundary Precipitation

Low- and high-angle boundaries present structural differences which can effect the nature of heterogeneous nucleation occurring on these defects. A generic high-angle boundary has high interfacial energy and a very tightly spaced array of dislocations. On the contrary, a low-angle boundary (either tilt or twist) has low interfacial energy and a loosely spaced array of dislocations. The results of this study show that the boride precipitate density at low-angle boundaries is much greater than at high-angle boundaries. However, the low-angle boundary precipitates are generally about half the size of the high-angle boundary borides. This observation leads one to consider that heterogeneous nucleation of the borides at the high-angle boundaries occurs with a smaller activation barrier than at low-angle boundaries. The high-angle boundary borides are larger because precipitation has occurred at an earlier time in the solid than at low-angle boundaries. The high-angle boundary borides coarsen while the low-angle boundary borides are just beginning to nucleate and grow. Ostwald ripening of the low-angle boundary precipitates is hindered by low temperatures of the ribbon. This precipitation scenario is consistent with the observed structures, provided that the assumption of solid state nucleation is accepted. Solid state nucleation arguments are presented in the next section.

The exact nature of the nucleation site for boride precipitation in these alloys remains unknown. Two approaches can be taken to rationalize differences in precipitate nucleation at high- and low-angle boundaries. Classically, the high-angle

boundary energy is much greater than low-angle boundary energy. Following the formulation of Cahn (31), the grain boundary precipitate is considered to consist of two truncated spheres as shown in fig. 24a. The interfacial dihedral angle  $\theta$  is determined from the relationship  $\cos \theta = \frac{\sigma_{\alpha\alpha}}{2\sigma_{\alpha\beta}}$ , where  $\sigma_{\alpha\alpha}$  is the grain boundary energy and  $\sigma_{\alpha\beta}$  is the boride-matrix interphase boundary energy. The heterogeneous nucleation rate on boundaries may be written as  $v_I^B = c \exp (-\Delta G_C^B/kT)$  (32), where  $v_I^B$  is the heterogeneous nucleation rate,  $c$  a constant,  $\Delta G_C^B$  is the activation barrier for boundary nucleation,  $k$  and  $T$  have their usual meaning. In fig. 24b a plot of normalized activation energy as a function of  $\cos \theta$  is given. Quickly one sees that the larger  $\cos \theta$ , indicating larger grain boundary energies, the lower the activation energy, and hence higher nucleation rates. This is entirely in agreement with the results of the current study; nucleation rates are much greater on the high angle boundaries because of the high interfacial energy. A second approach to the nucleation event would involve a discrete defect model for such events. Since the exact nature of the boride-matrix interface is unknown, this topic will not be pursued.

#### 5.4 Borides

A known and fixed orientation relationship between second phase particles and the surrounding matrix is indicative of at least liquid-solid interfacial precipitation and more likely solid state precipitation. If the second phase particles discretely line all boundaries in a system and there are no intra-

granular precipitates, then precipitation involving the liquid state is limited to the final instant in which two liquid-solid interfaces meet laterally. This occurs over a very short time and hence is an improbable event kinetically.

The microstructures of alloys 71 and 72 show regions where only solid state boride precipitation is plausible and other regions where liquid-solid interfacial precipitation is possible. For alloy 71, boride precipitation was observed primarily at boundaries, although there are interdendritic regions near the free surface with high boride density. Extensive boundary precipitation of borides also occurred in alloy 72, but several regions of interdendritic precipitation were observed. From the parallelism of moire fringe contrast, strength of the boride reflections in electron diffraction patterns, and the fact that several borides for a given grain "light up" in dark field when a boride reflection is used, it can be safely assumed that all borides have an orientation relationship with the matrix. This indicates that grain boundary boride precipitation occurs in the solid state. However, the possibility of liquid-solid interfacial nucleation for interdendritic precipitates cannot be excluded. A careful microstructural investigation of the interdendritic regions may shed light on the nature of the nucleation event.

## 5.5 Model for Lateral Microstructural Features

Concave polygons and concave grain shapes present local excesses in boundary length for a contained area. This can be extended to three dimensions; concave polyhedrons present local

excesses in surface area for a contained volume. The local excess area can be reduced by curvature driven boundary migration to straighten out curved or concave regions of boundary. The spatial location of a grain boundary can be stabilized by the presence of incoherent particles. A local minimum in inter-

\*-----  
This can also be the case for coherent precipitates, but the boundary geometry becomes more complex. This is a weak effect due to the low interfacial energy associated with coherent precipitates.

-----  
facial area and energy is achieved when a boundary intersects the effective equator of such particles. This simple process amounts to what is commonly known as grain boundary pinning and is responsible for the microstructural stability of innumerable alloy systems. The role of boundary pinning by boride precipitates and the effect on grain shapes are considered in this section.

Recalling the microstructures near the center and free surface of alloys 71 and 72, it was shown that overall grain shapes were concave and there were boundary regions with radii of curvature less than  $0.2\text{ }\mu\text{m}$ . The grain shapes near the free surface of alloy 70 were also concave. The grain faces of alloy 70 were shown to be straight. Grain shapes, for the most part, near the wheel side and in the ribbon center are convex for alloy 70, with straight boundaries. This is how the boundaries of alloy 70 shall be considered for the following model.

Vast amounts of research have been devoted to consideration of the structure of a moving liquid-solid interface. Research of this nature yields valuable information on the resulting microstructure, that is, whether it will be homogeneous, cellular or

dendritic. Less research has been devoted to how lateral interfaces meet, what that lateral solid shape is prior to impingement, and what happens to newly formed grain boundaries during cooling. To this author's knowledge, in fact, no such study has been carried out. When the grain shapes and boundary structures of alloys 71 and 72 are examined, one wonders why such irregularities exist. Coupling experimental results and thought experiments, a model can be formulated to describe the observed structural features.

To begin, consider the case where there are shape perturbations at the liquid-solid interface in the form of either cellular nodes or dendrites. Now as a thought experiment, consider the lateral structure of such shape perturbations, there are no symmetry limitations on this shape. That is, wavy or irregular cells and dendrites are permissible. Nothing dictates that boundaries have to be straight when irregularly shaped interfacial perturbations, or different grains, meet laterally. Even if the shape perturbations are circularly symmetric, two adjacent grains may differ slightly in size. The large node represents a lower chemical potential for the transformation and hence a higher growth rate. The large node essentially grows part way around the smaller adjacent cell, this is illustrated in fig. 25. The resulting grain boundary curves around the location of the smaller cell. Consider two additional situations; is there ever a case for non-plane front growth that straight grain boundaries form as a result of lateral impingement of cells? The more extreme case of dendritic freezing is easier to visualize. In this case, dendrites of different orientation intermix leading to

rough boundary shapes. Several other scenarios could be devised to rationalize curved boundaries and irregular grain shapes, but the principle point is that such events are physically plausible.

Once in the solid state, a curved boundary can either migrate (straightening) or be pinned. Pinning can be accomplished by either discrete second phase particles or by rapid quenching (herein called kinetic pinning). With this in hand, it is proposed that the grain boundaries in alloy 70 were initially very wavy but quickly straightened during cooling. The boundaries of alloys 71 and 72 were also curved just after solidification but maintained their irregular shapes during cooling. It is not anticipated that cooling rates vary significantly between any of these alloys, so it must be concluded that the boundary structures of alloys 71 and 72 are stabilized by the presence of discrete second phase particles--namely boride precipitates. A crucial feature of this model is that boride precipitation occurs quickly and in the solid state. Hence, using sound arguments, a straightforward model for lateral microstructural features, which is physically consistent with observed microstructures, has been presented. The model is schematically shown in fig. 25b.

## 5.6 Chemical Analysis by STEM

Quantitative analytical electron microscopy is limited to simple systems such as binaries and ternaries. For more liberally alloyed systems, such as complex heat-resistant alloys, compensation for x-ray fluorescence and absorption becomes too complicated to treat quantitatively. Therefore only qualitative results were reported.

The results are consistent with the observed microstructure. A slight degree of molybdenum and chromium segregation to boundaries was observed for the reference alloy. In the boride-precipitating alloy 71, a slight depletion of molybdenum and chromium at the grain boundaries is consistent with the fact that the borides are chromium and molybdenum rich. This is completely analogous to sensitization of stainless steels.

The fact that there is no variation in concentration of substitutional alloying elements through a ribbon thickness does not preclude the possibility of 'macrosegregation' of boron. Unfortunately, boron is undetectable at these low solid solution concentrations by means of analytical electron microscopy. Measurement of boride density as a function of location in a ribbon may show trends toward macrosegregation. This is convoluted, however, by the possibility of solute trapping near the wheel side.

## 6. Summary and Conclusion

1. The 'macrostructure' of the melt-spun ribbons generally displayed three characteristic regions: a fine chill zone near the wheel side, columnar grains in the ribbon center, and dendritic grains near the free surface. These features were shown to be analogous to those in large scale castings.
2. The observed tilt of the columnar dendritic structure into the casting direction is consistent with flow considerations. That is, growth is always promoted opposite to net adjacent fluid flow.
3. Alloy 70, the low boron alloy, displayed no definite boride precipitation. Equiaxed grains were observed near the wheel side and in the ribbon center. Subgrain formation was observed near the ribbon free surface--indicating the probability of cellular solidification near the top of the ribbons.
4. Alloys 71 and 72 displayed a slight degree of subgrain formation near the wheel side. The structures became dendritic near the ribbon free surface. Extensive boundary boride precipitation was observed at all locations in the ribbons. Further, in dendritic regions, local areas with exceptionally high boride density were observed.
5. Boride precipitation at grain boundaries occurs heterogeneously and with a lower activation barrier at high-angle boundaries than low-angle boundaries.
6. All boride precipitation in these alloys involves at least

one solid interface because of the observed precipitate-matrix orientation relationship.

7. It is proposed that when liquid-solid interfaces meet laterally, the resulting grain boundary is wavy and irregularly shaped. The boundary can either migrate or be pinned. The high-angle boundaries of alloy 70 are suspected to have straightened during cooling, whereas the high-angle boundaries of alloys 71 and 72 were pinned by boride precipitates.

ORIGINAL PAGE IS  
OF POOR QUALITY

## 7. Directions for Future Research

Few scientific investigations, if any, are self-enclosing. This study is surely no exception. So the following suggestions for future work are made.

- A cursory study of the mechanical and physical properties of alloys 70, 71, and 72 is suggested to provide information on the potential service utility of these alloys.

- Aging studies are proposed to provide information on microstructural response to thermal treatments. In this manner, upper temperature limits may be established for microstructural resistance to coarsening.

- 'Macrosegregation' of boron may occur in these alloys. Conventional analytic techniques such as STEM, SEM, electron microprobe are all undersirable for this problem either because of low sensitivity or poor spatial resolution.

One possible technique for detecting boron, however, is secondary ion mass spectroscopy (SIMS). With SIMS a fine probe of primary ions such as  $\text{He}^+$  is focused onto a polished specimen surface. The primary ions collide with the specimen, leading to ion fragments being emitted from the specimen surface. These secondary ions are tuned through a mass spectrometer to a detector. Lateral spatial resolution is that of the probe diameter and depth resolution is on the order of atomic layers. Probes as fine as 400 Å in diameter can be formed. Furthermore, elements of all Z can be detected.

Since we are concerned with boron macrosegregation, it is of little importance whether boron is in solid solution or tied up in precipitates. An ideal experiment would be to nickel plate a

ribbon, mount and polish it edge on, and then run perhaps ten sets of SIMS counts at approximately six to ten different levels of the ribbon thickness. A probe diameter of 1 to 2  $\mu\text{m}$  would be ideal for it would sample averaged structure.  $\text{B}^+$  counts could be ratioed to total counts. In this manner, the through thickness variation of boron level could be determined.

- A parallel study is proposed for a simpler alloy system, but one which is alloyed with an interstitial element which tends to segregate to boundaries, and a second alloying element which ties up with the interstitial (such a system might be Ni-Ti-B, Ni-Mo-C, . . . ). The goal of such a study would be in determining velocity-driving force expressions for grain boundary motion. Using such an expression, calculations of extent of grain boundary motion during post-solidification quenching could be performed. The calculated grain boundary mobility could be compared with boundary shapes observed in a series of rapidly solidified alloys. More exotic experiments such as quenching onto a hot substrate could also be performed to alter the post-solidification cooling rate.

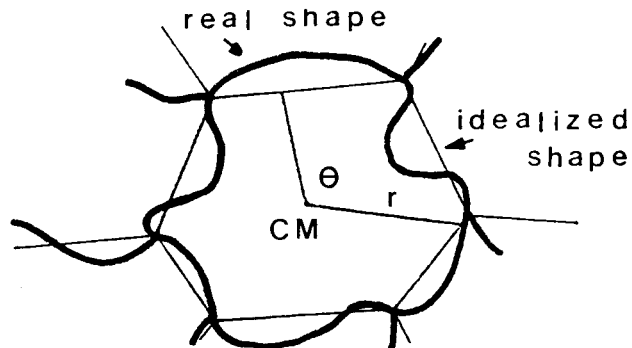
## Bibliography

1. R. F. Decker and C. T. Hagel, in The Superalloys (ed. C. T. Sims and W. C. Hagel), Wiley, 1972, 34.
2. T. F. Kelly and J. B. Vander Sande, in Chemistry and Physics of Rapidly Solidified Materials (ed. B. J. Berkowitz and R. O. Scattergood), AIME, 1983, 35-47.
3. R. Raj and M. F. Ashby, Met. Trans. A, 2 (1971), 1113-1127.
4. T. R. Anantharamn, C. Suryanarayana, J. Mat. Sci., 6 (1971), 1111-1135.
5. H. Jones, in Rapidly Quenched Metals -- Second International Conference (ed. N. J. Grant and B. Giessen), MIT, 1976, 1-27.
6. M. Cohen and R. Mehrabian, in Rapid Solidification Processing, Principles and Technologies III (ed. R. Mehrabian), NBS, 1983, 1-27.
7. M. Cohen, B. H. Kear, and R. Mehrabian, Rapid Solidification Processing Principles and Technologies II (ed. R. Mehrabian, B. Kear, and M. Cohen), Claitors, 1980, 1-23.
8. J. V. Wood, P. F. Mills, J. K. Bingham, and J. V. Bee, Met. Trans. A, 10 (1979), 575-584.
9. H. A. Davies, N. Shohoji, And D. H. Warrington, in Rapid Solidification Processing Principles and Technologies II (ed. R. Mehrabian), Claitors, 1980, 153-164.
10. M. C. Flemings, C. M. Adams, E. E. Huckle, H. F. Taylor, Trans. AFS, 64 (1956), 636-639.
11. E. S. Micksch, Trans. Met. Soc. AIME, 245 (1967), 2059-2072.
12. K. Murakami, T. Fujiyama, A. Koike, and T. Okamoto, Acta Met., 31, 9 (1983), 1425-1432.
13. S. C. Huang, E. L. Hall, and T. K. Glasgow, in Rapid Solidification Processing Principles and Technologies III (ed. R. Mehrabian), NBS, 1982, 377-383.
14. F. Duflos and J. F. Stohr, J. Mat. Sci. 17 (1982), 3641-3652.
15. S. C. Huang and A. M. Ritter, in Chemistry and Physics of Rapidly Solidified Materials (ed. B. J. Berkowitz and R. O. Scattergood), AIME, 1983, 25-34.
16. M. Tanaka and S. Kawasaki, J. Nucl. Mat., 45 (1972-73), 82-86, and 48 (1973), 360-364.

17. N. Bozkurt, A. Geckinli, and M. Geckinli, *Mat. Sci. and Eng.*, 57 (1983), 181-186.
18. J. M. Walsh and B. H. Kear, *Met. Trans. A*, 6 (1975), 226-229.
19. W. C. Leslie, *The Physical Metallurgy of Steels*, McGraw Hill, 1982, 269-281.
20. R. C. Ruhl and M. Cohen, *Trans. Met. Soc. AIME*, 245 (1969), 253-257.
21. R. F. Decker, and J. W. Freeman, *Trans. Met. Soc. AIME*, 218 (1960), 277-285.
22. K. H. Johnson, in *Local Density Approximations in Quantum Chemistry* (ed. J. P. Dahl and J. Avery), Plenum, 1984, 487-514.
23. R. P. Messmer and R. P. Briant, *Acta Met*, 30 (1982), 457-467.
24. R. Kiesling, *Acta Chem. Scan.*, 4 (1950), 209-227.
25. H. Nowotny, in *Electronic Structure and Alloy Chemistry of the Transition Elements* (ed. P. Beck), Wiley, 1963, 204.
26. W. J. Boesch and H. B. Canada, *J. of Met.*, April 1968, 46-50.
27. H. J. Beattie, *Acta Cryst.*, 11 (1958), 607-609.
28. S. C. Huang, E. L. Hall, and T. K. Glasgow, in *Rapid Solidification Processing Principles and Technologies III* (ed. R. Mehrabian), NBS, 1982, 377-383.
29. H. Segal, Eng. thesis--Dept. of Mat. Sci. and Eng., MIT, 1983.
30. E. Gutierrez, research in progress at MIT.
31. J. W. Cahn, *Acta Met.*, 4 (1956), 449-459.
32. J. W. Christian, *The Theory of Phase Transformations in Metals and Alloys*, 2nd ed., Pergamon, 1975, 450.

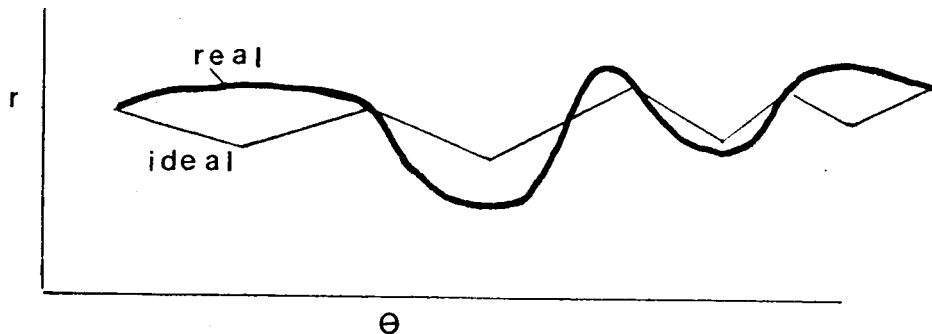
## Appendix

Define the reference grain as the convex shape formed from absolute triple points as reference points. From this define an effective center of mass, CM.

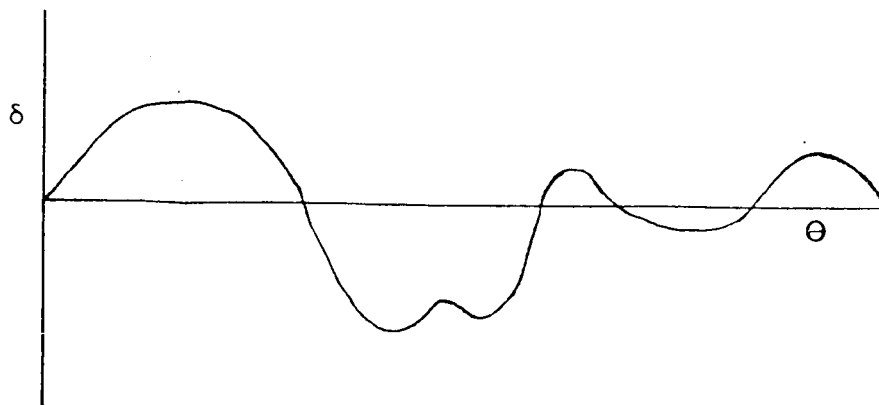


Convex, or idealized, grain shape formed from absolute triple points.

Defining an arbitrary starting point, plot the radial dependence of the distance from the grain center, CM, to the grain boundary of the idealized grain shape (black ink). Also plot the radial distance for the real grain shape (red ink).



The difference gives the grain boundary amplitude,  $\delta$ .



ORIGINAL PAGE IS  
OF POOR QUALITY



Figure 1 -- Longitudinal 'macrostructure' of alloy 70. The wheel side is at the bottom of the figure; free surface at the top. Casting direction was from left to right (from ref. 29).

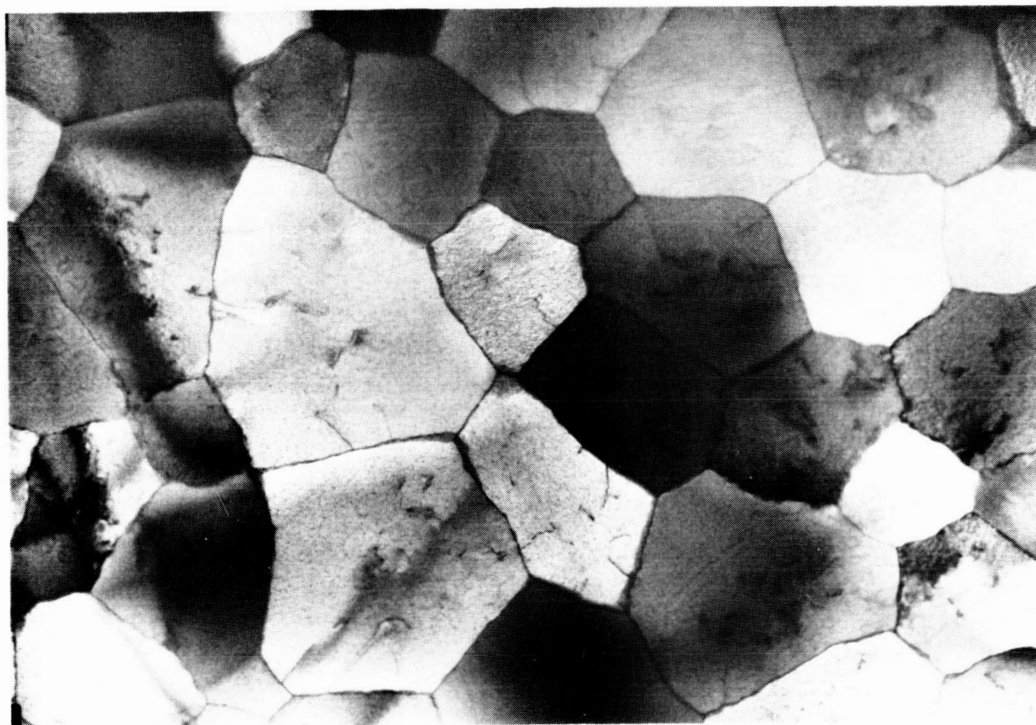


Figure 2 -- Longitudinal 'macrostructure' of alloy 71. The sample geometry is the same as fig. 1 (from ref. 29).

ORIGINAL PAGE IS  
OF POOR QUALITY



Figure 3 -- Longitudinal 'macrostructure' of alloy 72. The sample geometry is the same as fig. 1 (from ref. 29).



1.0 μm

Figure 4 -- Overall microstructure near the wheel side (WS) of alloy 70.



Bright Field

0.5 $\mu$ m



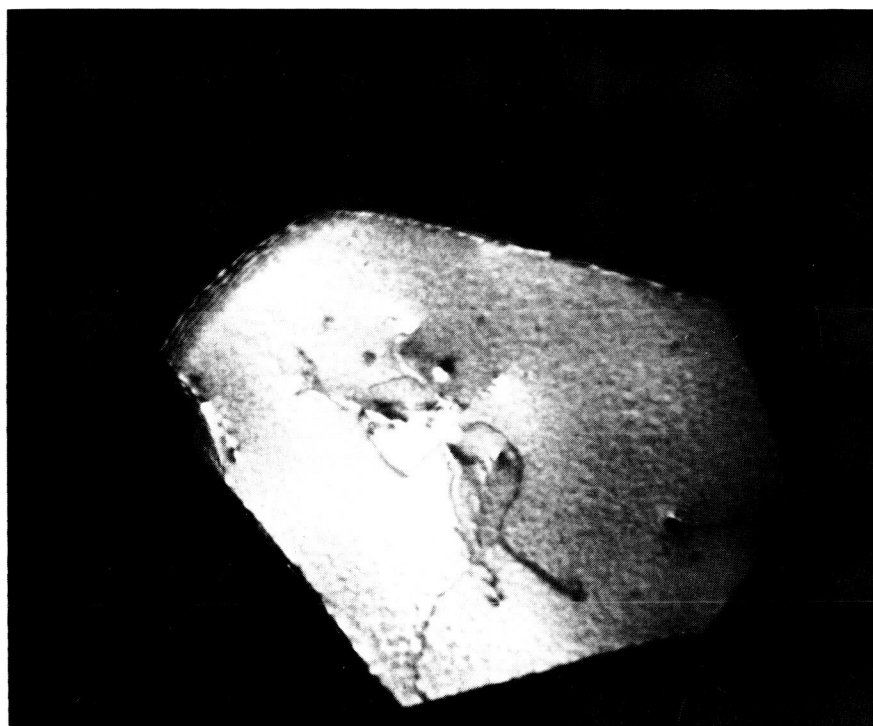
Dark Field

Figure 5 -- Bright field/dark field (BF/DF) pair from a region near the ribbon wheel side of alloy 70. A (220) matrix reflection was used to form the DF image.



Bright Field

0.5 $\mu$ m



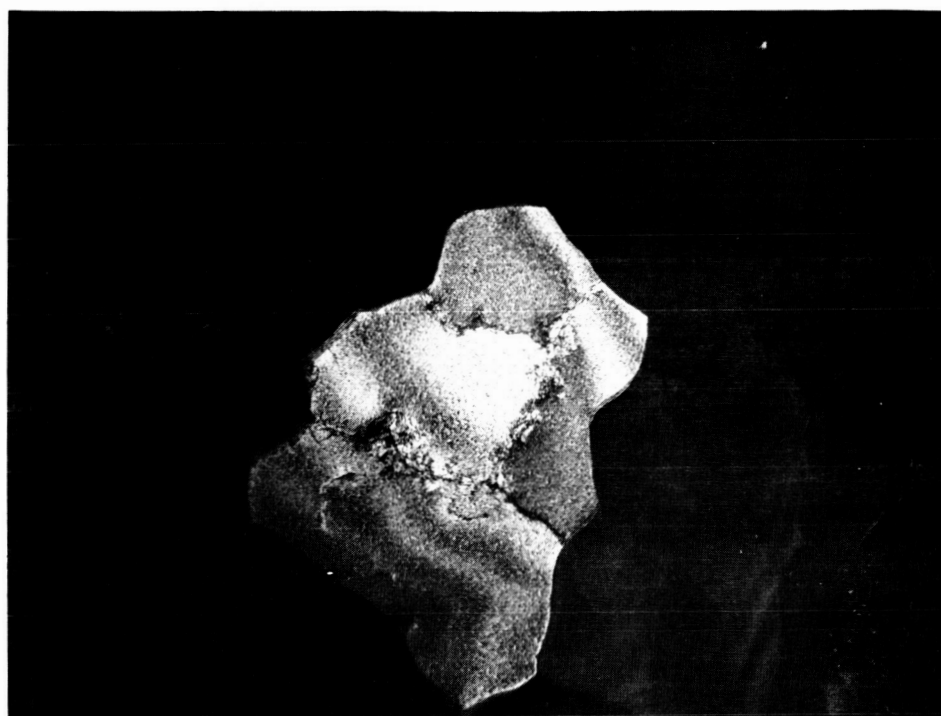
Dark Field

Figure 6 -- BF/DF pair for a region in the ribbon center (C) of alloy 70. A (220) matrix reflection was used to form the DF image.



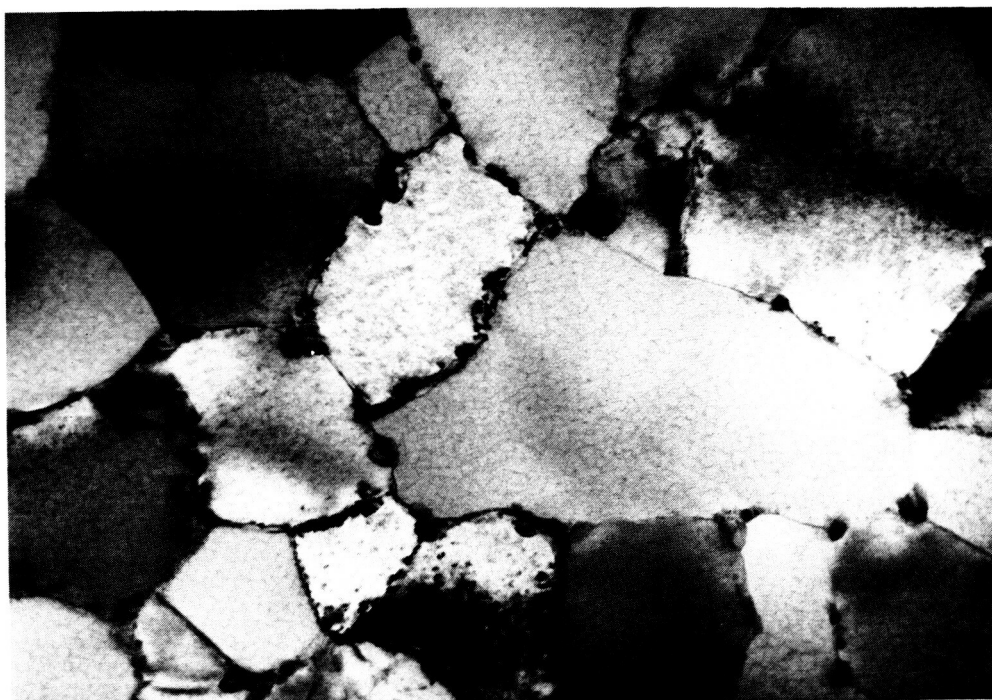
Bright Field

1.0μm



Dark Field

Figure 7 -- BF/DF pair for a region near the ribbon free surface (FS) of alloy 70. A (200) matrix reflection was used to form the DF image.



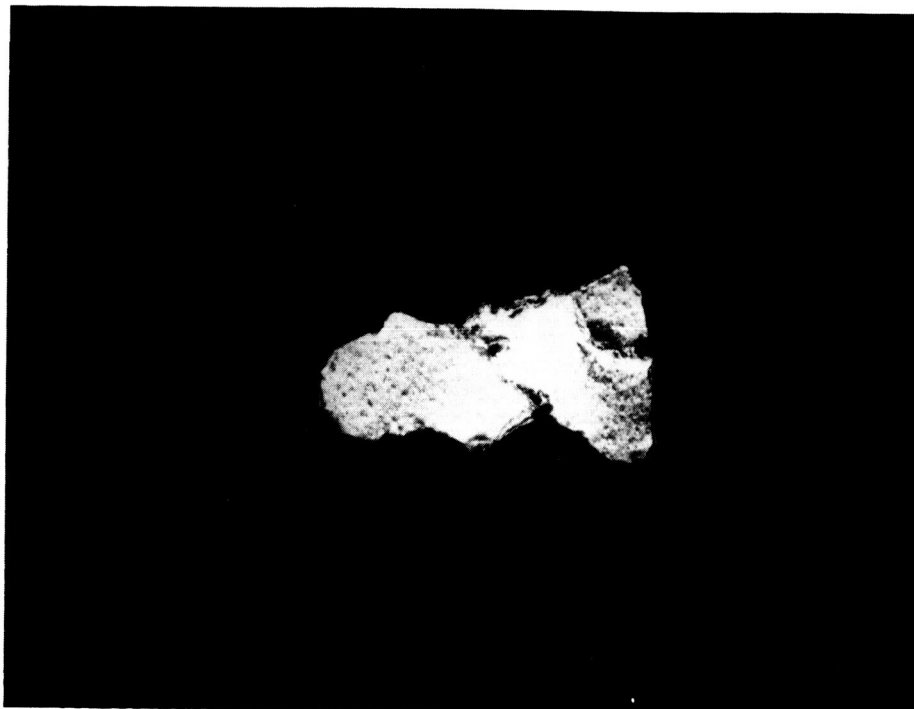
0.25 $\mu$ m

Figure 8 -- Overall structure near the wheel side of alloy 71.



Bright Field

0.5 $\mu$ m



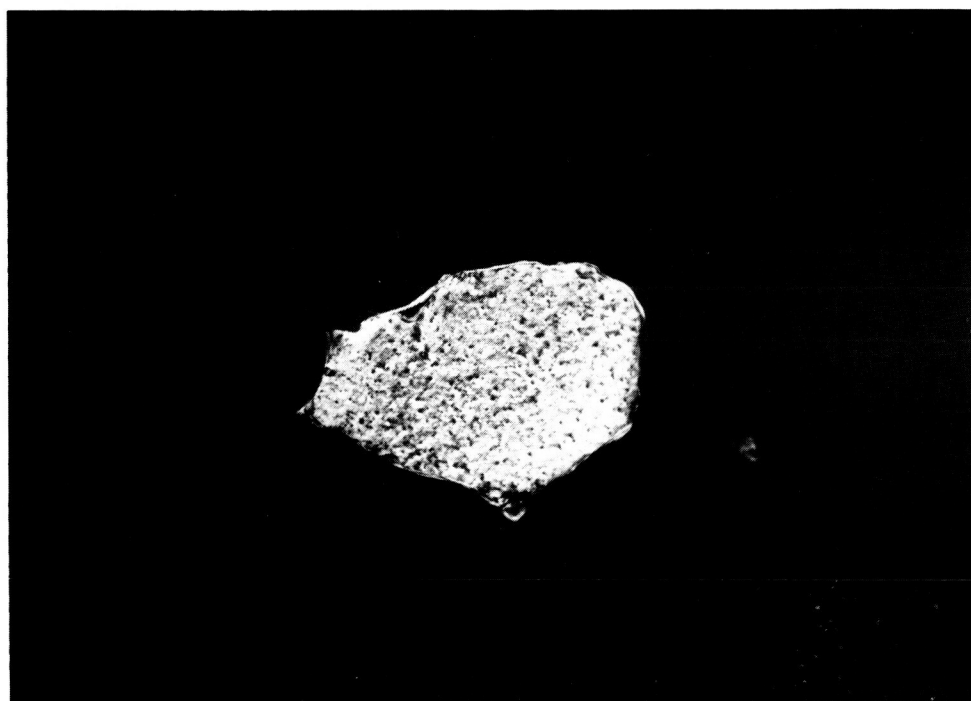
Dark Field

Figure 9a -- BF/DF pair for a region near the ribbon WS of alloy 71. A (220) matrix reflection was used to form the DF image.



Bright Field

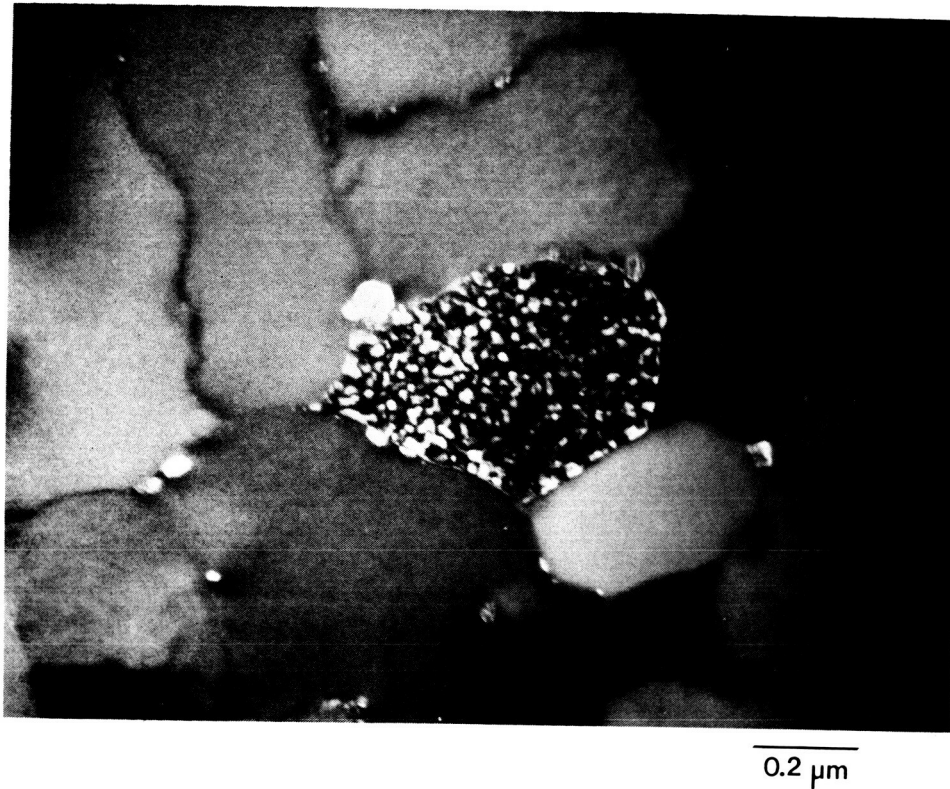
0.2  $\mu\text{m}$



Dark Field

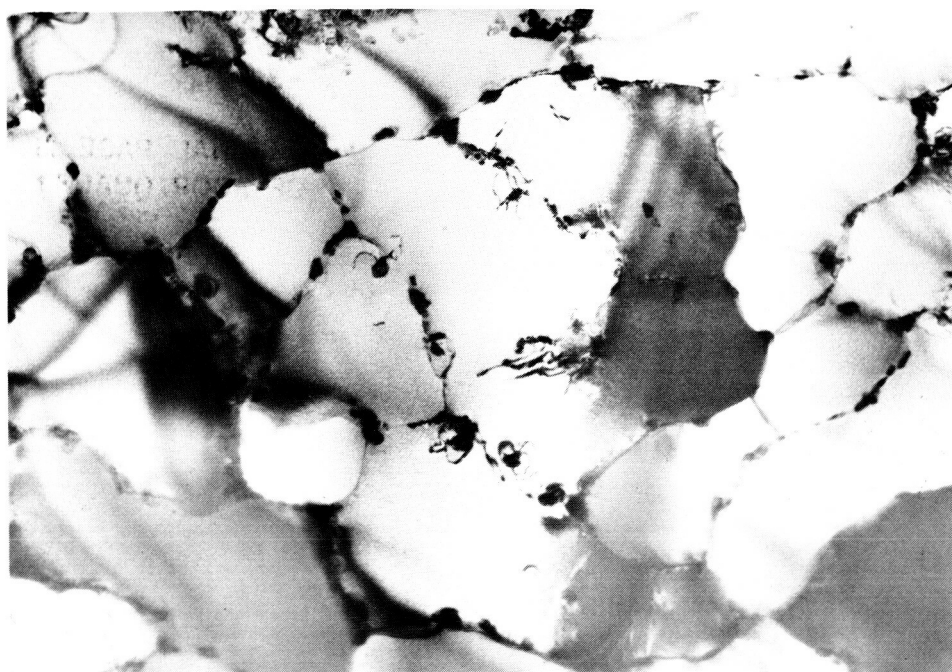
Figure 9b -- BF/DF set for a region near the ribbon WS of alloy 71. A (200) matrix reflection was used to form the matrix dark field image. A (100)  $\gamma'$  reflection was used to form the superlattice dark field image.

ORIGINAL PAGE IS  
OF POOR QUALITY



Superlattice Dark Field

Figure 9b continued.



Bright Field

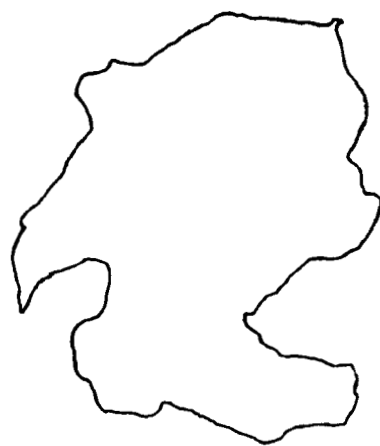
0.5μm



Dark Field

Figure 10 -- BF/DF pair from a region in ribbon C of alloy 71. (220) matrix reflection was used to form the dark field image. A sketch of the reflecting grain shape is given on the following page.

A  
A



Sketch of Reflecting Grain Shape

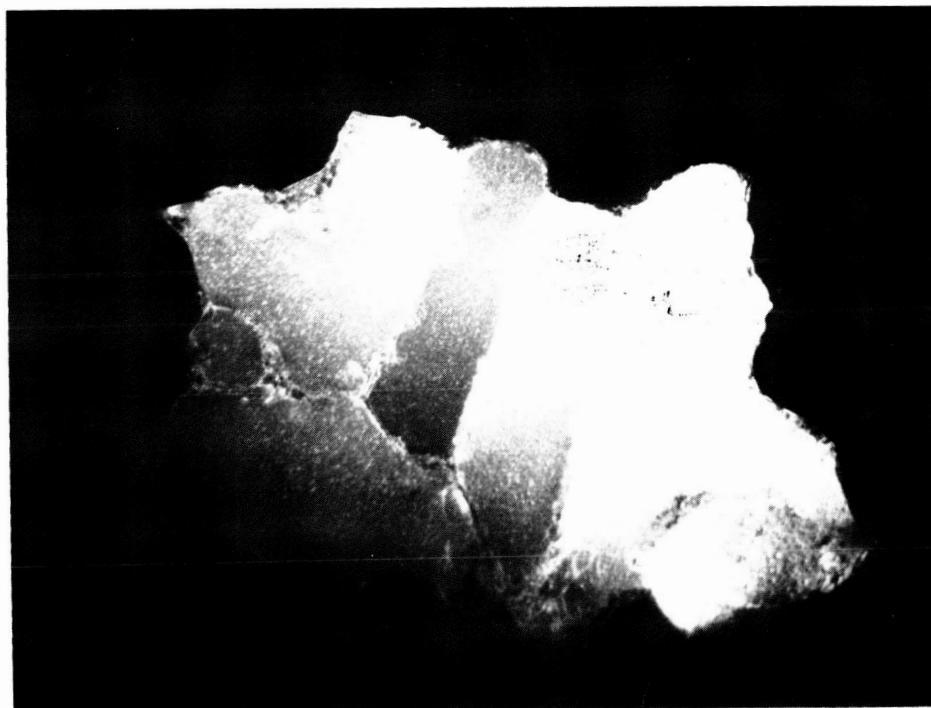
Figure 10 continued.

ORIGINAL PAGE IS  
OF POOR QUALITY



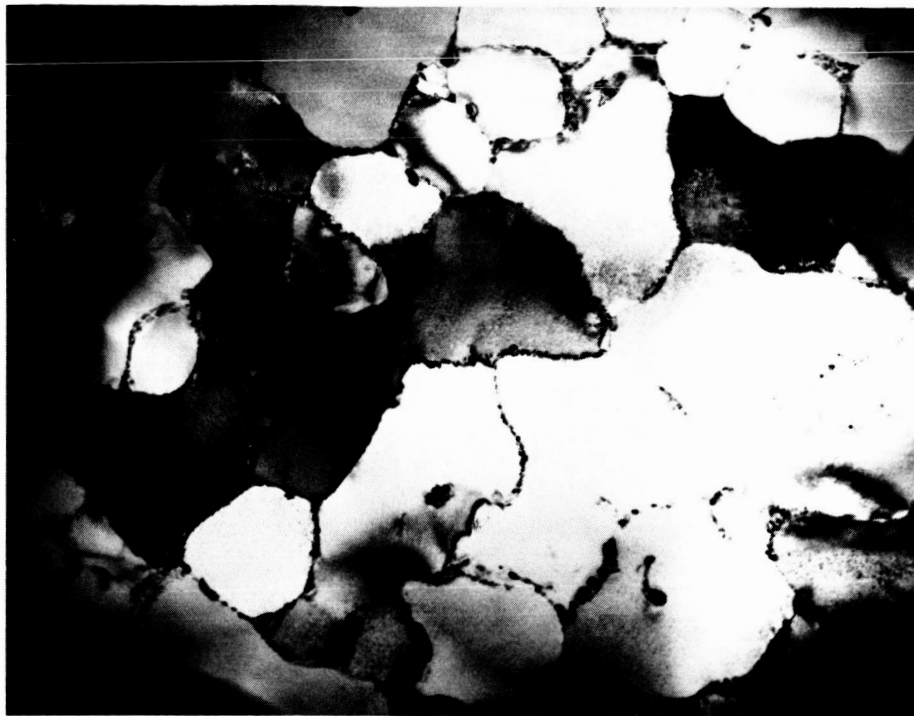
Bright Field

0.5 $\mu$ m



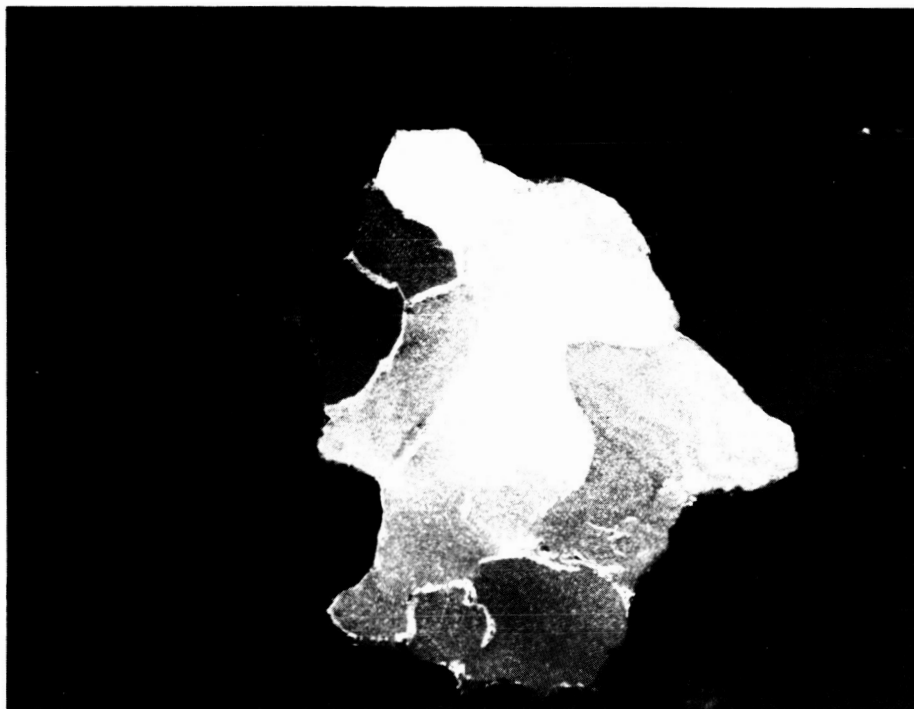
Dark Field

Figure 11a -- BF/DF pair for a region near ribbon FS of alloy 71.  
A (220) matrix reflection was used to form the dark field image.



Bright Field

1.0 $\mu$ m



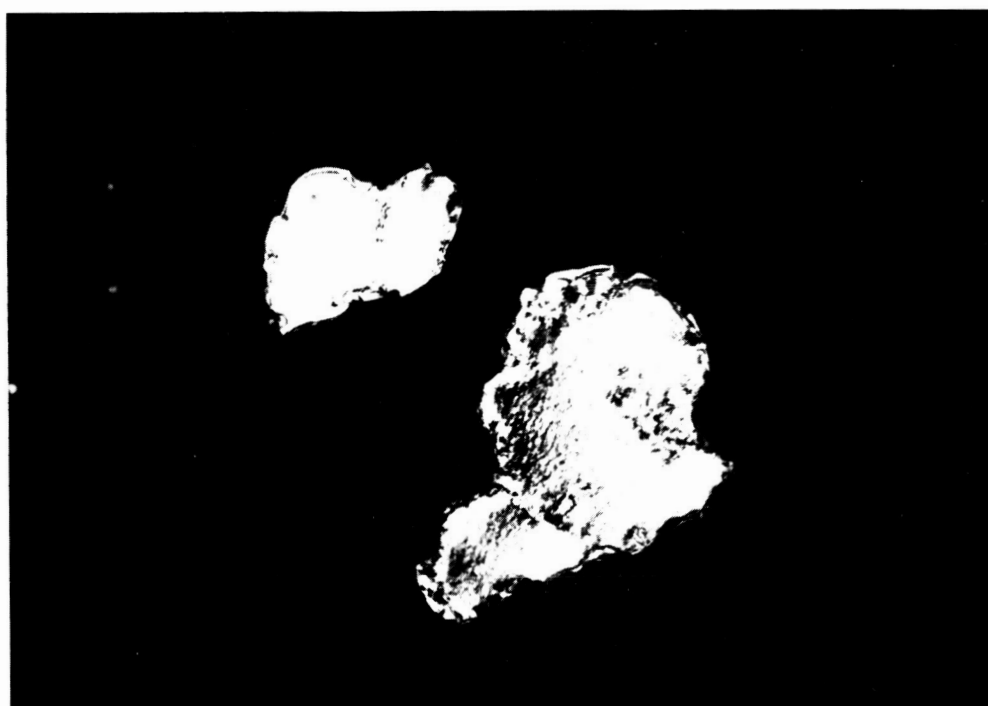
Dark Field

Figure 11b -- BF/DF pair for a region near ribbon FS of alloy 71.  
A (311) matrix reflection was used to form the dark field image.



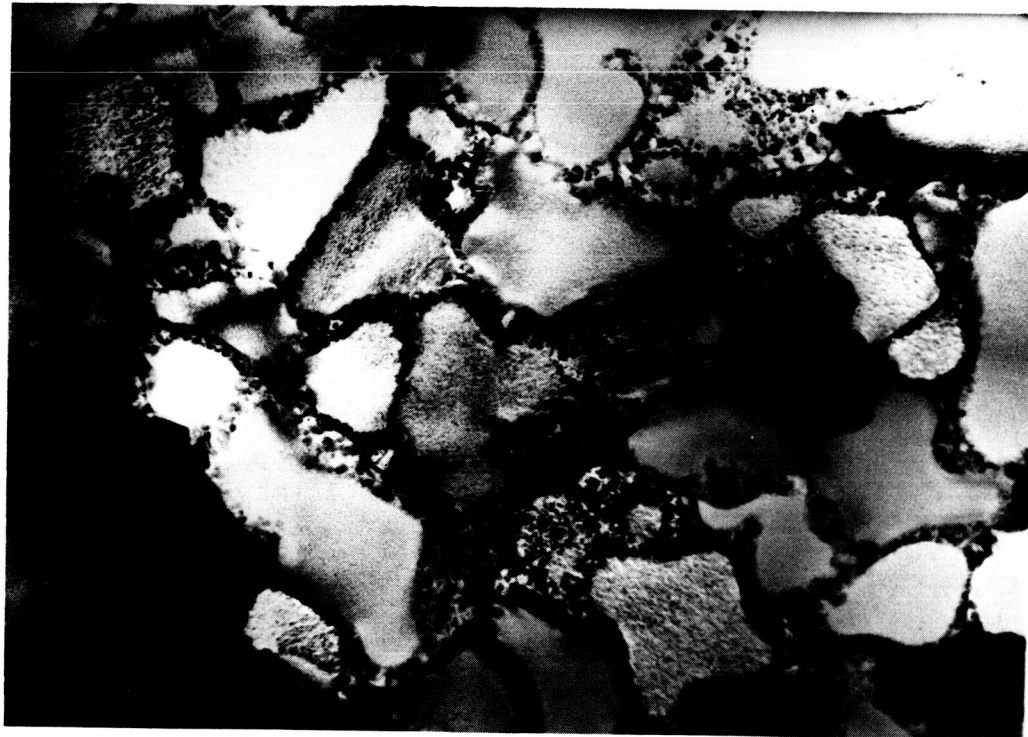
Bright Field

0.2  $\mu\text{m}$



Dark Field

Figure 12a -- BF/DF pair from a region near the ribbon WS of alloy 72. A (200) matrix reflection was used to form the DF image.



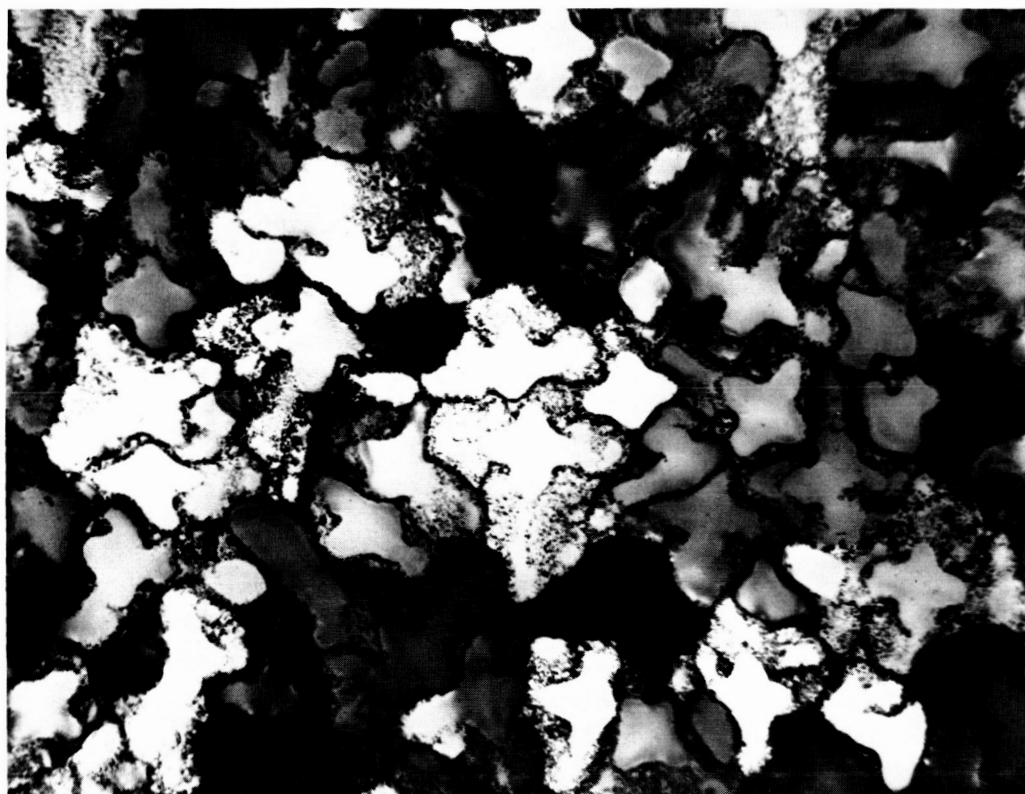
Bright Field

0.5 $\mu$ m



Dark Field

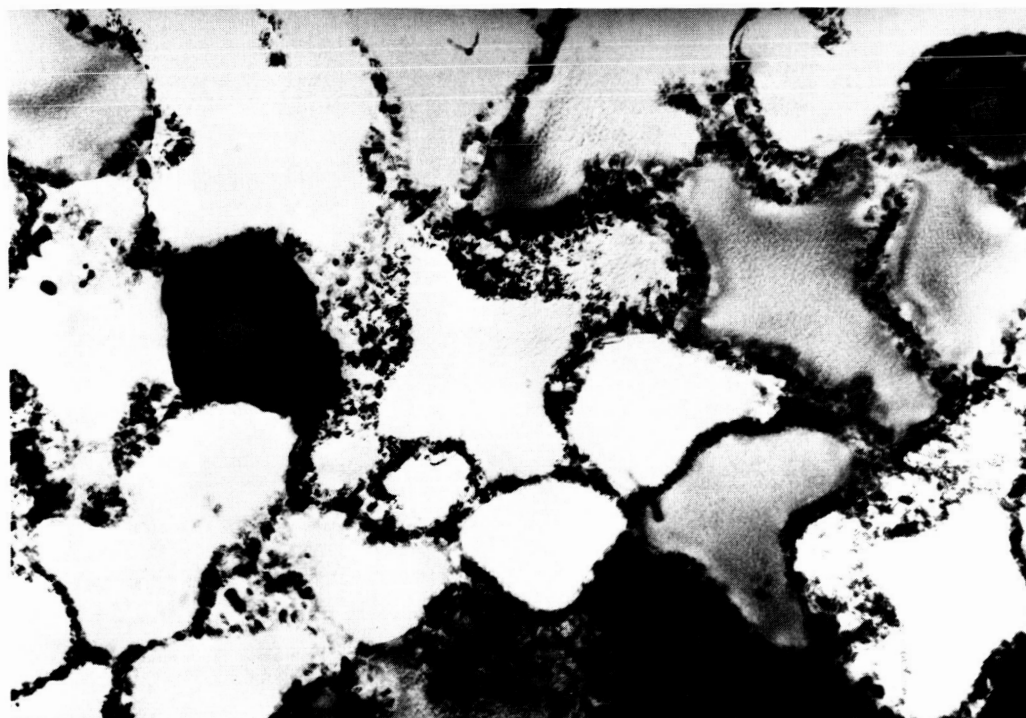
Figure 12b -- BF/DF pair from a region near the ribbon WS of alloy 72. A (200) matrix reflection was used to form the DF image.



1.0 $\mu$ m

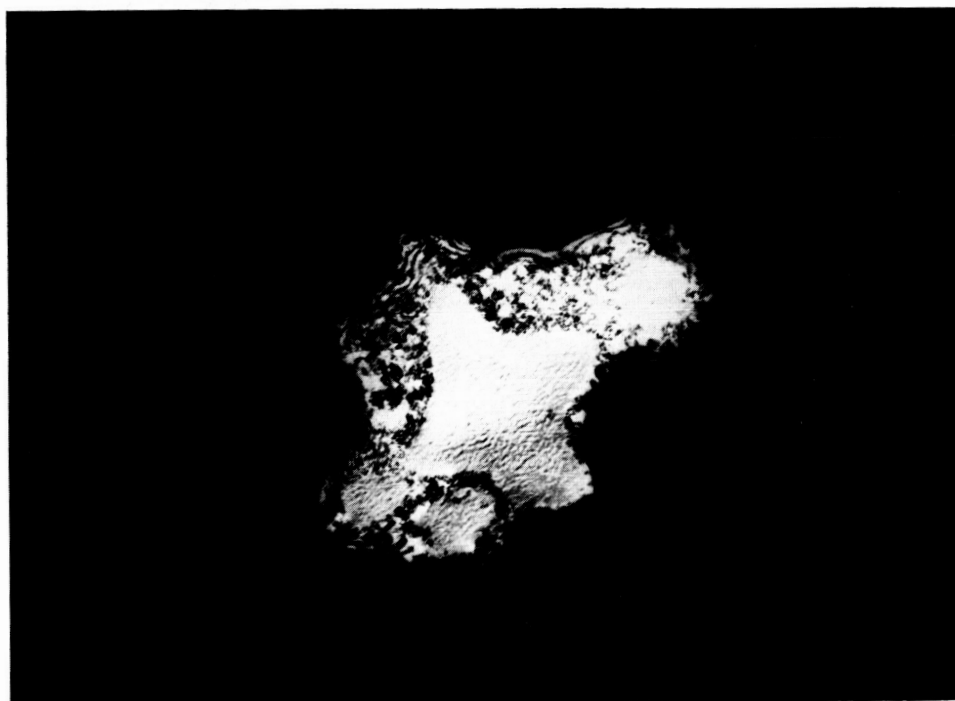
Fig. 13 -- Overall structure in the ribbon center of alloy 72.

ORIGINAL PAGE IS  
OF POOR QUALITY



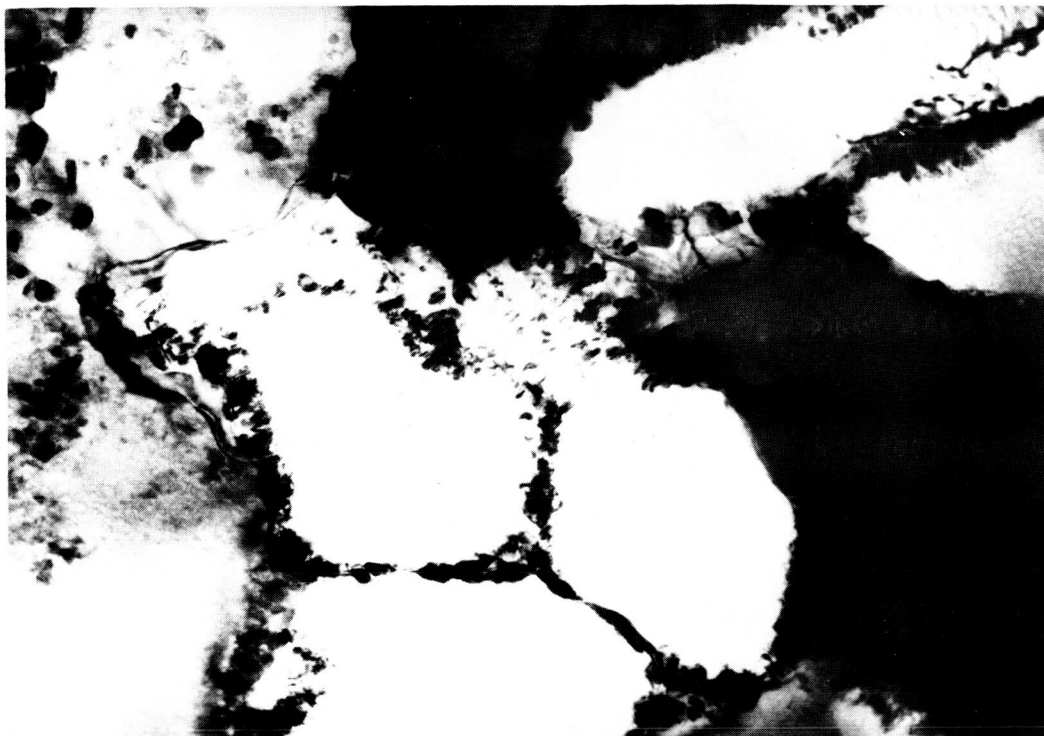
Bright Field

0.5  $\mu$ m



Dark Field

Figure 14a -- BF/DF pair from ribbon C of alloy 72. A (200) matrix reflection was used to form the dark field image.



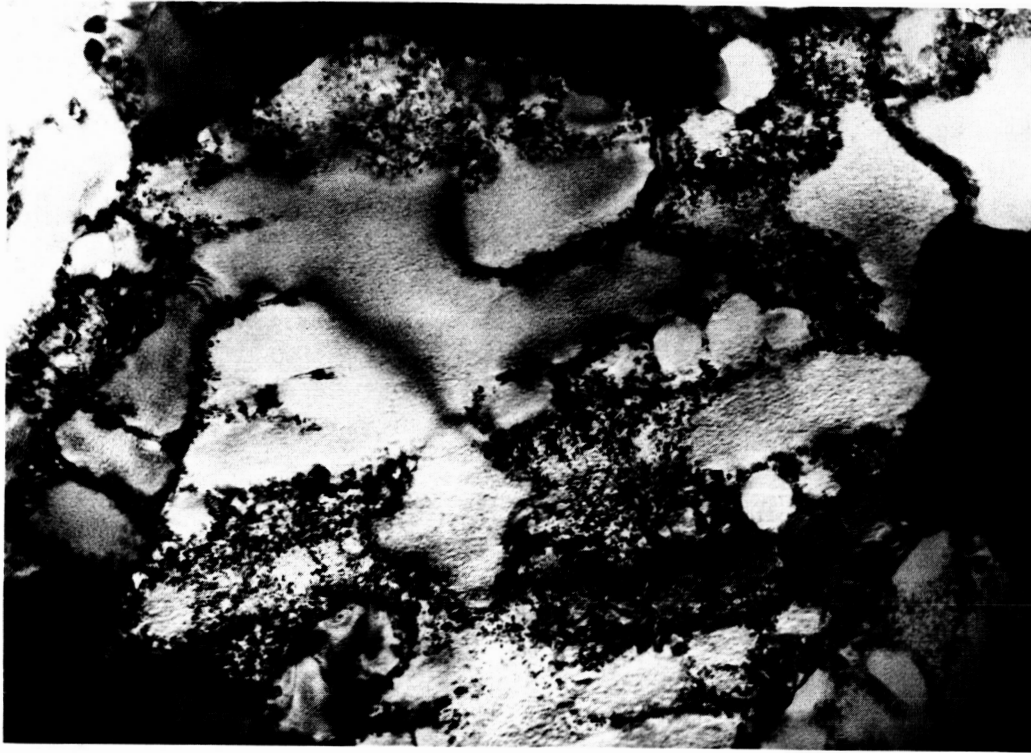
Bright Field

0.2  $\mu\text{m}$



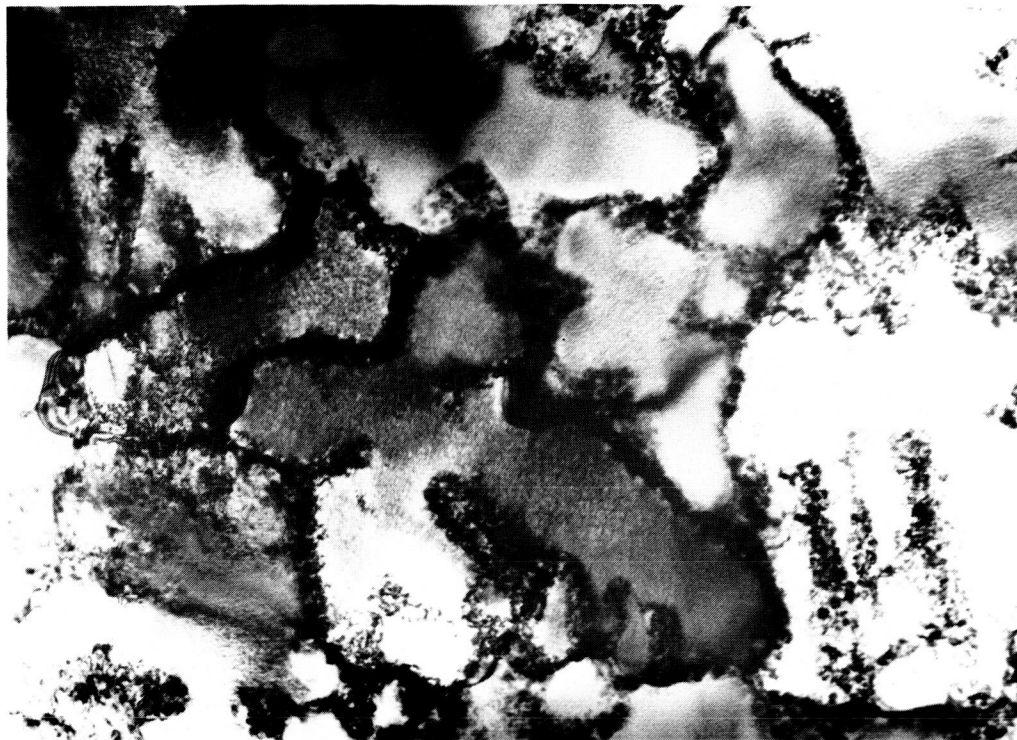
Dark Field

Figure 14b -- BF/DF pair from ribbon C of alloy 72. A (200) matrix reflection was used for the dark field image.



0.5 $\mu$ m

Figure 15 -- Overall structure near ribbon FS of alloy 72.



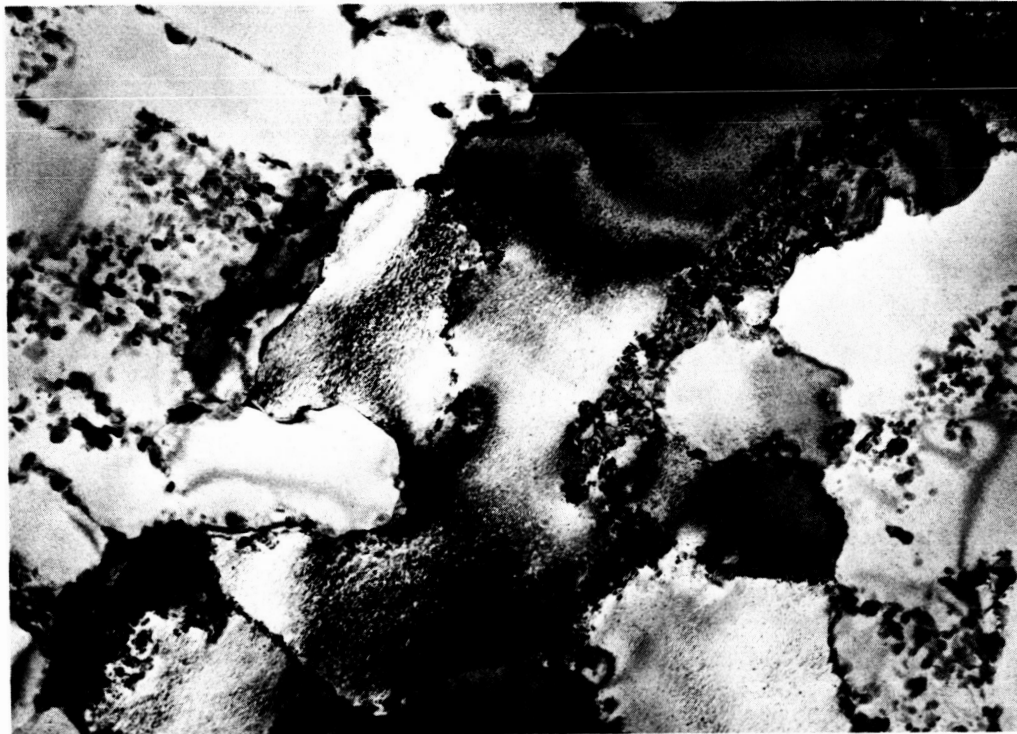
Bright Field

0.5 $\mu$ m



Dark Field

Figure 16a -- BF/DF pair from ribbon FS of alloy 72. A (220) matrix reflection was used to form the dark field image.



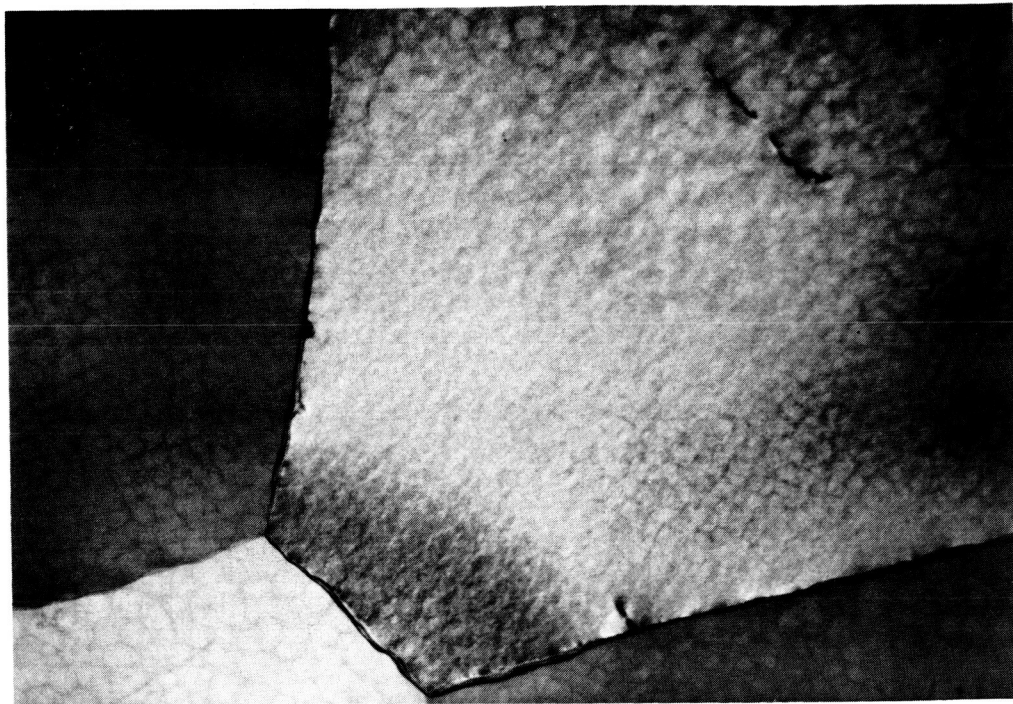
Bright Field

0.5 $\mu$ m



Dark Field

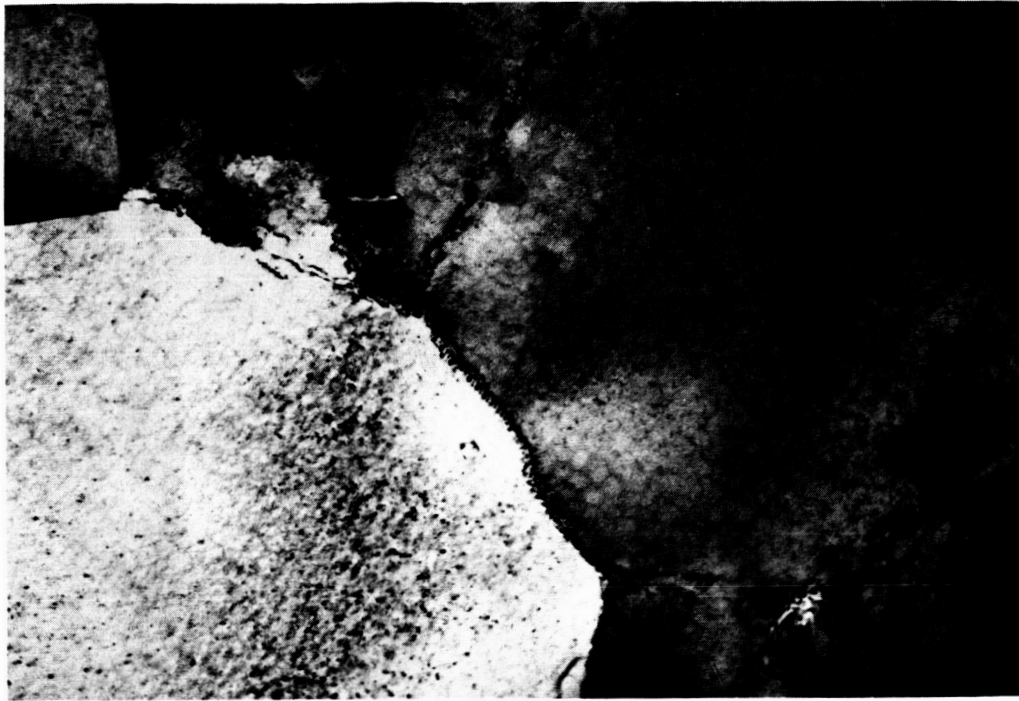
Figure 16b -- BF/DF pair from ribbon FS of alloy 72. A (220) matrix reflection was used to form the dark field image.



0.2  $\mu\text{m}$

Figure 17 -- High-angle grain boundaries in ribbon C of alloy 70.

ORIGINAL PAGE IS  
OF POOR QUALITY



0.2  $\mu$ m

Figure 18 -- Low-angle grain boundary near FS of alloy 70.  
Possible precipitation at the boundary should be noted.

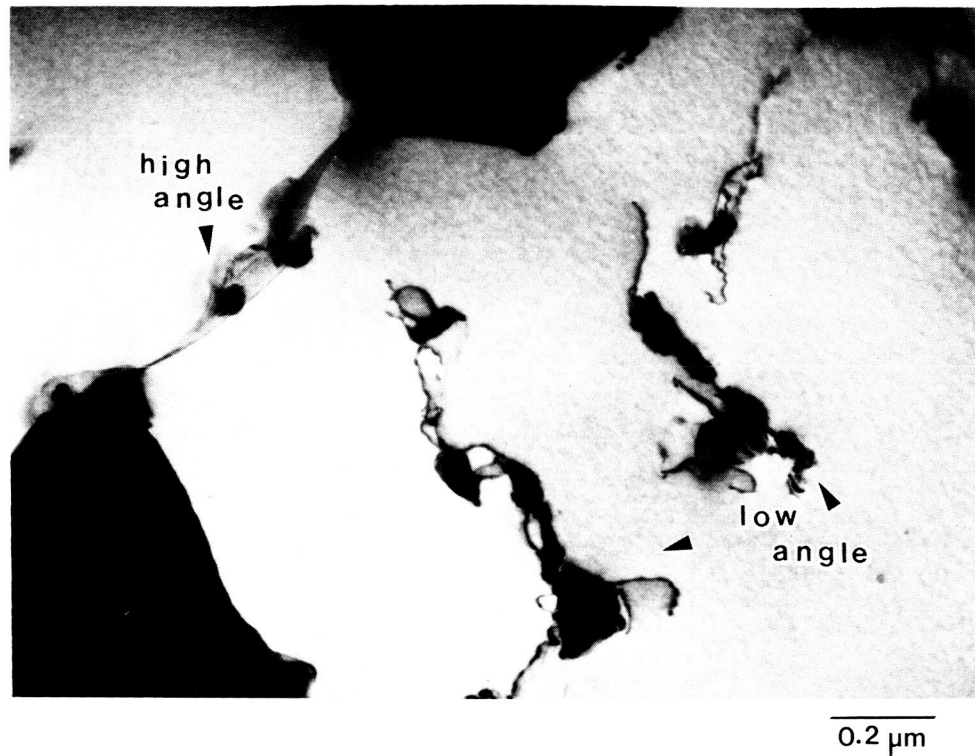


Figure 19 -- Low- and high-angle grain boundary precipitation in the ribbon C of alloy 71.

ORIGINAL PAGE IS  
OF POOR QUALITY

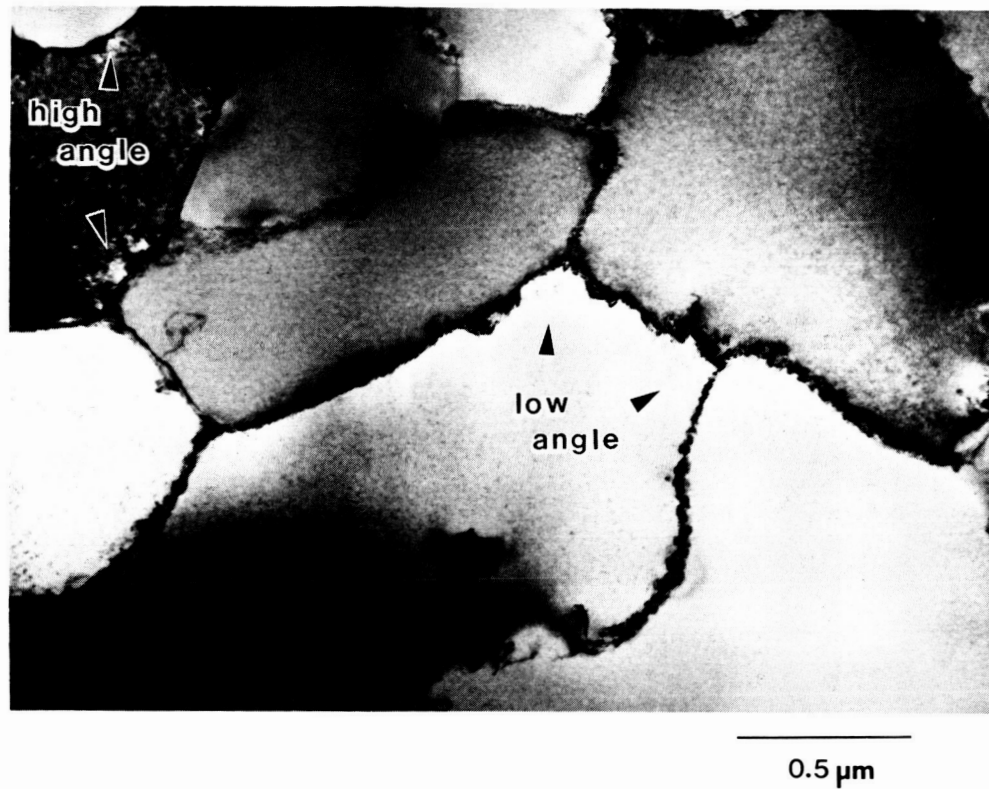
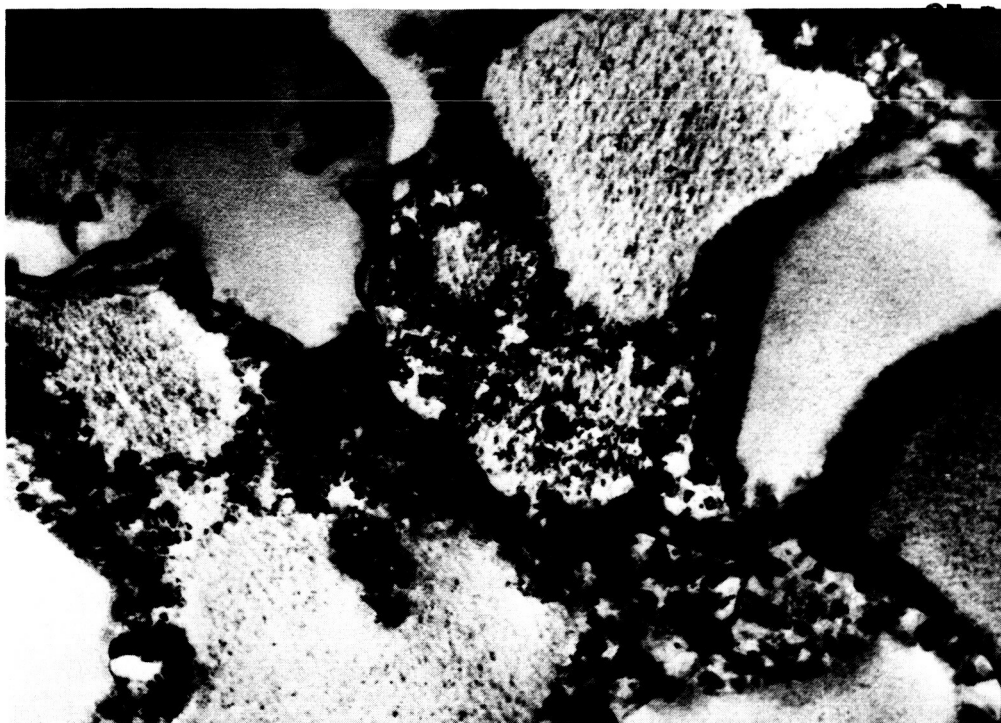


Figure 20a -- Low- and high-angle grain boundary precipitation near the ribbon FS of alloy 71.



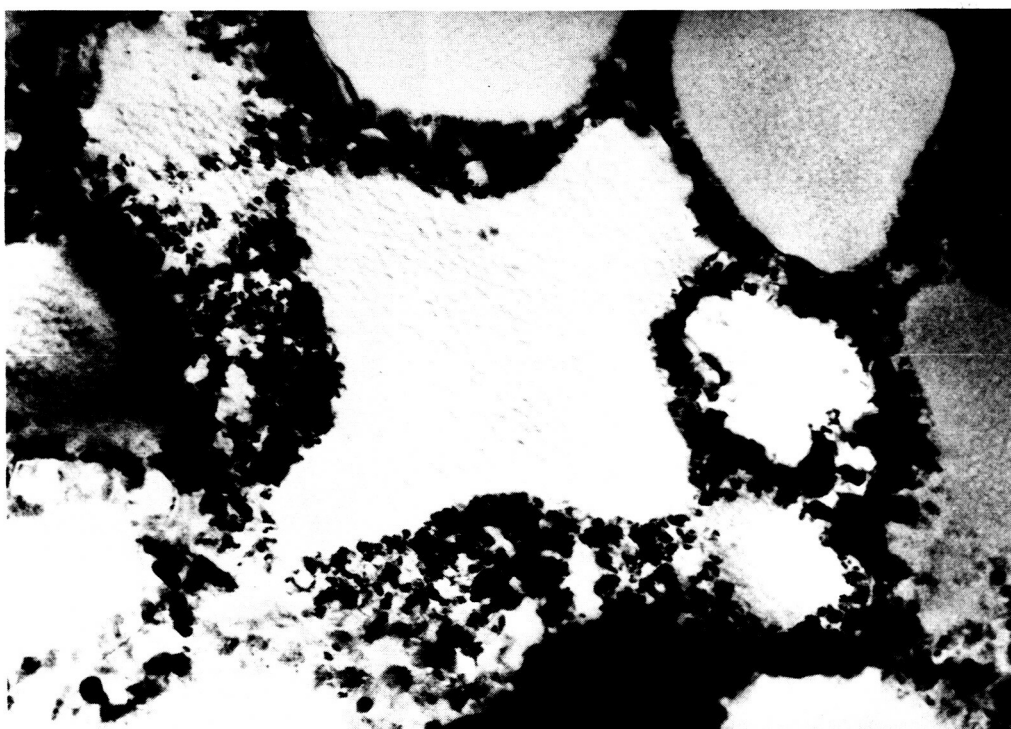
0.2 $\mu$ m

Figure 20b -- Low-angle boundary structure near the ribbon FS of alloy 71.



a.

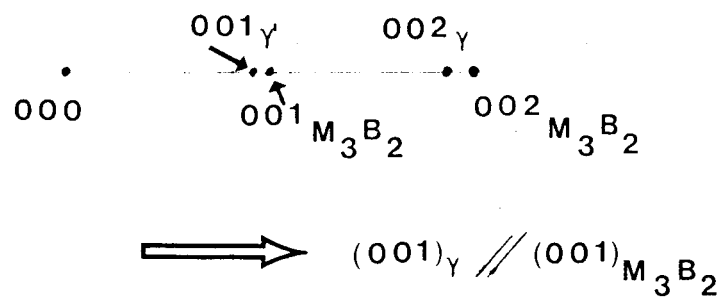
0.1µm



b.

Figure 21 -- Microstructure of alloy 72 showing local regions of high boride density; a. near ribbon WS. b. near ribbon center.

$$z = [x \times 0]$$



$$z = [001]$$

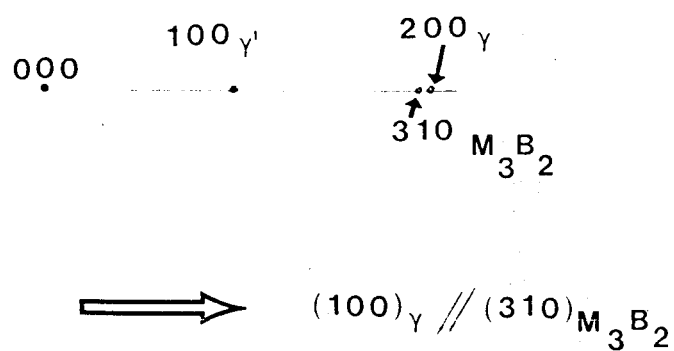


Figure 22 -- Schematic electron diffraction patterns depicting matrix-boride orientation relationship.

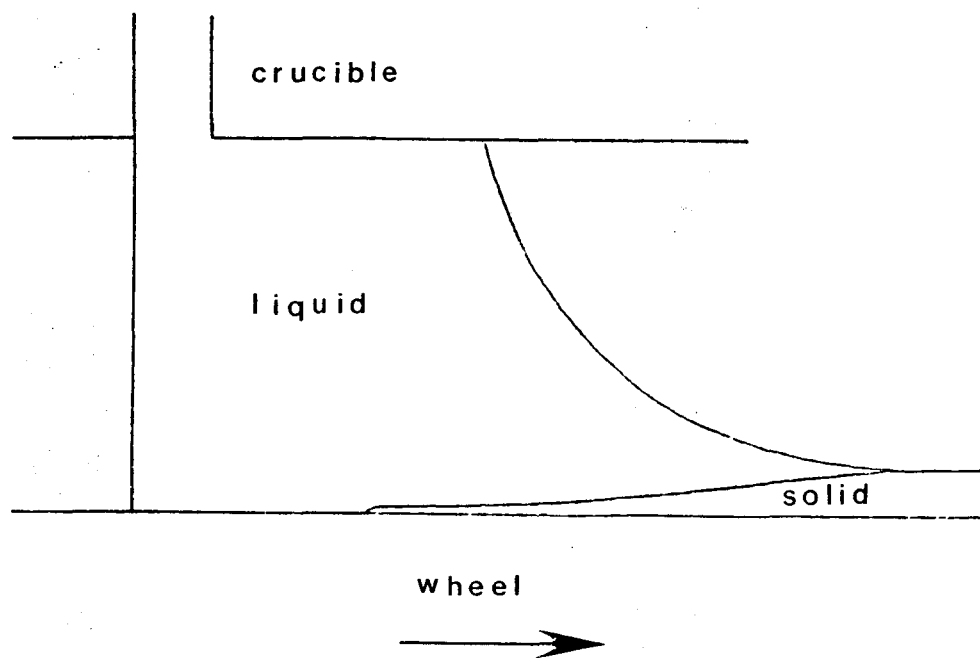
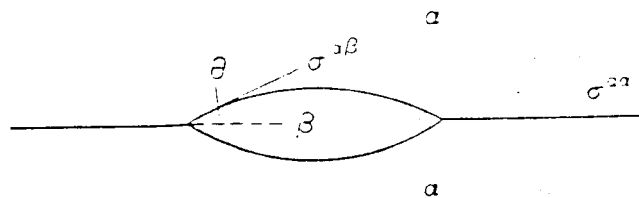
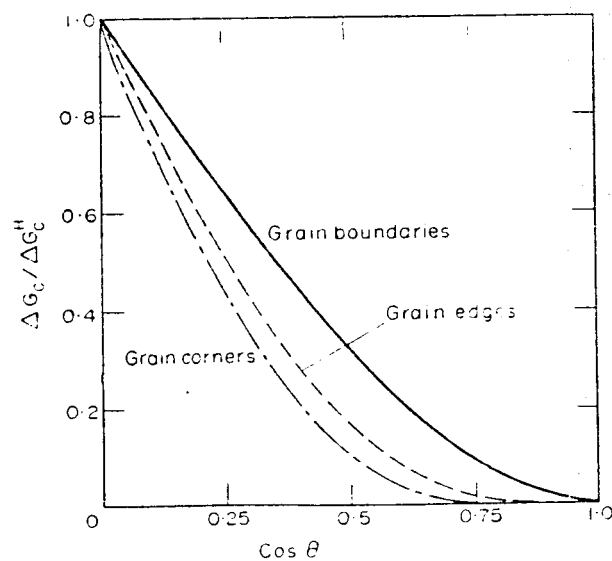


Figure 23 -- Schematic diagram of the planar-flow melt-spinning process.



a.



b.

Figure 24 -- a. Geometry of idealized grain boundary precipitate. b. The effect of the cosine of the wetting angle,  $\theta$ , on the normalized activation energy for nucleation on defects. ( $\Delta G_C^H$  is the critical homogeneous nucleation activation energy. From ref. 32, p. 454).

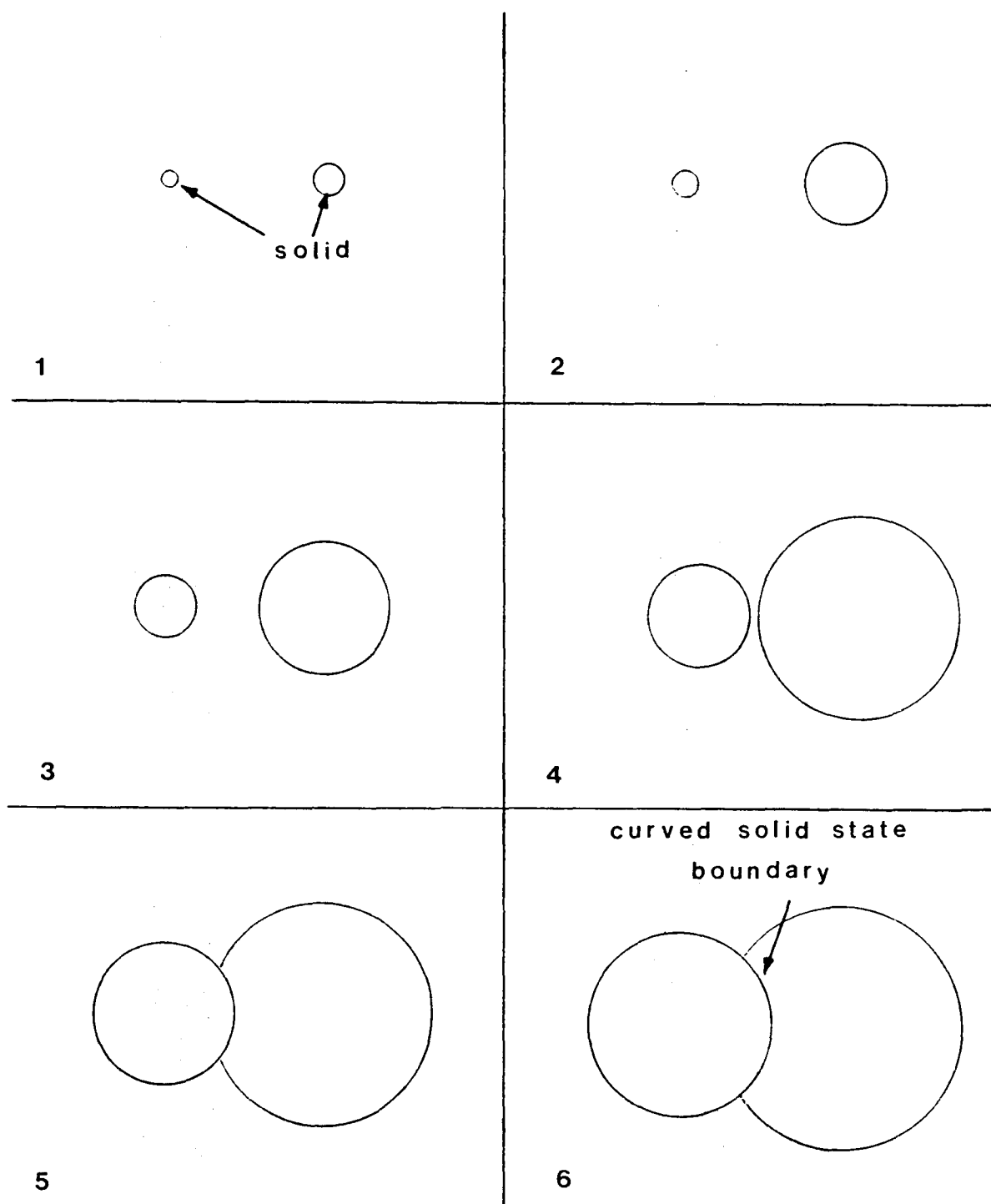


Figure 25a -- Sketch of competitive lateral growth of perturbations at the liquid-solid interface leading to a curved grain boundary. The 'plane' of the liquid-solid interface is parallel to the plane of the figure.

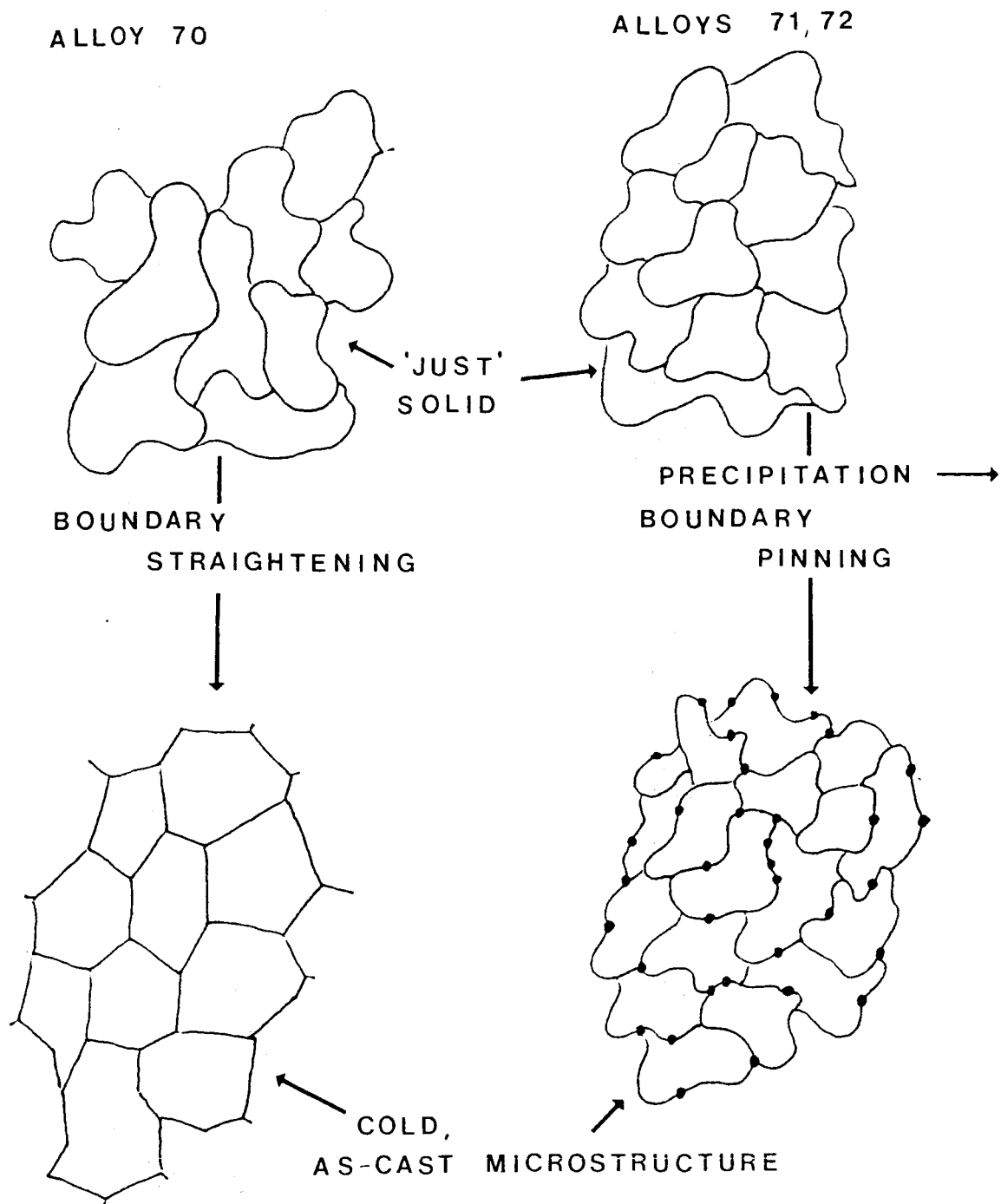


Figure 25b -- Schematic diagram of proposed solidification sequence.

1. Report No. <b>NASA CR-179553</b>		2. Government Accession No.		3. Recipient's Catalog No.	
4. Title and Subtitle  <b>A Study of the Microstructure of a Rapidly Solidified Nickel-Base Superalloy Modified With Boron</b>				5. Report Date <b>November 1986</b>	
				6. Performing Organization Code	
7. Author(s)  <b>James S. Speck</b>				8. Performing Organization Report No.  <b>None</b>	
				10. Work Unit No.  <b>505-33-62</b>	
9. Performing Organization Name and Address  <b>Massachusetts Institute of Technology Department of Materials Science and Engineering Cambridge, Massachusetts 02139</b>				11. Contract or Grant No.  <b>NAG3-365</b>	
				13. Type of Report and Period Covered  <b>Contractor Report Final</b>	
12. Sponsoring Agency Name and Address  <b>National Aeronautics and Space Administration Lewis Research Center Cleveland, Ohio 44135</b>				14. Sponsoring Agency Code	
15. Supplementary Notes  <b>Project Manager, Thomas K. Glasgow, Materials Division, NASA Lewis Research Center. This report was submitted as a thesis in partial fulfillment of the requirements for the degree of Master of Science at the Massachusetts Institute of Technology in 1985.</b>					
16. Abstract  <b>The microstructures of melt-spun superalloy ribbons with variable boron levels have been studied by transmission electron microscopy. The base alloy was of approximate composition Ni-11% Cr-5%Mo-5%Al-4%Ti with boron levels of 0.06, 0.12, and 0.60 percent (all by weight). 30 <math>\mu</math>m thick ribbons display an equiaxed chill zone near the wheel contact side which develops into primary dendrite arms in the ribbon center. Secondary dendrite arms are observed near the ribbon free surface. In the higher boron bearing alloys, boride precipitates are observed along grain boundaries. A concerted effort has been made to elucidate true grain shapes by the use of bright field/dark field microscopy. In the low boron alloy, grain shapes are often convex, and grain faces are flat. Boundary faces frequently have large curvature, and grain shapes form concave polygons in the higher boron level alloys. It is proposed that just after solidification, in all of the alloys studied, grain shapes were initially concave and boundaries were wavy. Boundary straightening is presumed to occur on cooling in the low boron alloy. Boundary migration is precluded in the higher boron alloys by "fast" precipitation of borides at internal interfaces.</b>					
17. Key Words (Suggested by Author(s))  <b>Superalloys Rapid solidification Coarsening</b>			18. Distribution Statement  <b>Unclassified - unlimited STAR Category 26</b>		
19. Security Classif. (of this report)  <b>Unclassified</b>		20. Security Classif. (of this page)  <b>Unclassified</b>		22. Price*  <b>A05</b>	
				21. No. of pages  <b>82</b>	